Alma Mater Studiorum · Università di Bologna

Scuola di Scienze
Dipartimento di Fisica e Astronomia
Corso di Laurea in Fisica

Theoretical models and *ab initio* calculations of phonons

Relatore:
Prof. Cesare Franchini

Correlatore:
Dott. Luigi Ranalli

Presentata da:
Matteo Costa

Anno Accademico 2021/2022

Summary

Abstract

Questa tesi intende approfondire da un punto di vista, sia teorico sia computazionale, le proprietà fondamentali dei fononi. A tal fine, sono presentati i modelli quantistici di Einstein e di Debye che permettono la derivazione analitica degli osservabili macroscopici principali di un solido, come l'energia media e la capacità termica. Ciò è possibile tramite una trattazione meccano-statistica basata sull'approssimazione armonica dei modi normali di vibrazione degli ioni reticolari. Quindi, all'inizio si mostrano brevemente i risultati principali riguardanti l'oscillatore armonico quantistico. Successivamente, si approfondiscono i temi della dispersione fononica e della densità degli stati vibrazionali per reticoli cristallini 1D e 3D. Si ottiene che la prima non può essere considerata lineare se non nel limite di alte lunghezze d'onda, e che la seconda può presentare punti di singolarità correlati alla forma della relazione di dispersione. Infine, sono state svolte alcune analisi computazionali *ab initio* relative alla dispersione fononica, la densità degli stati vibrazionali e la frequenza di Debye del Carbonio (diamante) tramite i programmi VASP e Phonopy, confrontando i risultati con dati sperimentali presenti in letteratura.

Chapter 1

Introduction

Phonons are defined as quantized vibrations of atoms in a solid lattice along the normal modes of the system (3 per atom: 1 longitudinal and 2 transverse). These internal motions allow the crystal to store and transfer energy. As a consequence, they contribute to many macroscopic materials' properties, such as heat transfer, sound propagation in media and electrical resistance.
In the last decades, the phononic properties of materials have thus been studied in search of useful applications. Given the remarkable improvement in design, fabrication and characterization of materials from centimeter to nanometer scale, many technological innovations have been developed, both in the fields of sound and heat control. For example, just to list some of them, acoustic diodes (same as electronic diodes, but for sound waves) and cloaking shells (devices for the insulation of finite spatial regions from sound waves without altering them) have been realized using respectively 1D-3D phononic crystals that reflect sound waves with frequency in a precise range and metamaterials with inhomogeneous bulk modulus and mass density [1].
Focusing back in the phonons' nature, it can be proved (explicit demonstration in Section 2.1.2) that they can also be described as non-interacting and massless bosons, despite their experimental observation in interacting systems. So, phonons' mean occupation of a generic energy level obeys to the Bose-Einstein statistical distribution with zero chemical potential.
The thesis is divided in three chapters, whose content is detailed below.
In the **first chapter**, the most important theoretical models about phonons' properties are discussed, beginning with the treatment of 1D simple harmonic oscillators [2]-[3] to which the vibrational modes can be approximated if the amplitudes of atomic motions are enough small. Then, being the heat capacity an useful response function for macroscopic materials, both classical [2] and quantum procedures [3]-[4] for its determination are presented. However, the evidence of their critical issues and limitations makes it necessary to deepen the topics of phononic dispersion [4]-[2] and density of states [5], which indeed exhibit complicated and interrelated structures.

In the **second chapter**, the phononic properties of a fcc Bravais lattice of diamond Carbon are studied by performing *ab initio* calculations via VASP (acronym for Vienna Ab initio Simulation Package [6]-[7]-[8]) and post-process analyses via Phonopy [9]. Given the right Input files, the first of the two packages allows to compute an approximate solution to the many-body Schrödinger problem [10], whose theoretical basis is also presented in order to better understand the mechanisms hidden behind the numerical results of the program. While the other one uses the dynamical matrix to obtain the phonon frequencies along the chosen high symmetry paths in the first Brillouin zone. In this way, the *ab initio* calculated values for the phononic dispersion relation and the density of states are plotted and compared to the experimental data in [11] and [12].
At last, in the **third chapter**, one can find an overview of the main theoretical results and critical issues, followed by a summary of the *ab initio* calculations for the fcc Bravais lattice of diamond Carbon.

Chapter 2

Theoretical models

2.1 Harmonic approximation

If the N atoms in a crystal lattice vibrate with small amplitudes of oscillation from their equilibrium sites with respect to the average atomic distances, then the interaction potential, as well as the Hamiltonian, can be approximated to an harmonic form, which basically describes the $3N$ associated normal modes as 1D simple harmonic oscillators. However, a classical treatment is not enough to properly model the macroscopic properties of materials in the low and intermediate temperature ranges.
Therefore, first of all, the energy eigenvalue problem for such systems is discussed by a quantum approach, aiming at the determination of their well-known discrete and non-degenerate energy spectrum. Next, assuming the existence of a sufficiently large ensemble, some statistical quantities useful for the following sections are obtained.

2.1.1 Second quantization

Assuming as well known the Dirac notation of quantum mechanics, one can solve the energy eigenvalue problem for a 1D simple harmonic oscillator of mass m and frequency ω by introducing the annihilation and creation operators pair (respectively $\hat{a}$ and its adjoint $\hat{a}^\dagger$) as

$$\begin{cases} \hat{a} = \frac{1}{\sqrt{2m\hbar\omega}}(\hat{p} - im\omega\hat{q}) \\ \hat{a}^\dagger = \frac{1}{\sqrt{2m\hbar\omega}}(\hat{p} + im\omega\hat{q}) \end{cases} \tag{2.1.1.1}$$

in dependence on the position $\hat{q}$ and momentum operators $\hat{p}$ such that the following commutation relation is satisfied

$$[\hat{a}, \hat{a}^\dagger] = \hat{1}, \tag{2.1.1.2}$$

where $\hat{1}$ is the identity operator.
Directly from the annihilation and creation operators pair, it is possible to define the

number operator $\hat{N}$ as the product

$$\hat{N} = \hat{a}^\dagger \hat{a} \tag{2.1.1.3}$$

which obeys the commutation relations

$$\begin{cases} [\hat{N}, \hat{a}] = [\hat{a}^\dagger \hat{a}, \hat{a}] = [\hat{a}^\dagger, \hat{a}]\hat{a} + \hat{a}^\dagger[\hat{a}, \hat{a}] = -\hat{a} \\ [\hat{N}, \hat{a}^\dagger] = [\hat{a}^\dagger \hat{a}, \hat{a}^\dagger] = [\hat{a}^\dagger, \hat{a}^\dagger]\hat{a} + \hat{a}^\dagger[\hat{a}, \hat{a}^\dagger] = +\hat{a}^\dagger \end{cases} \tag{2.1.1.4}$$

due to the validity of Leibniz-like rules for commutator.
In the particular case of a 1D harmonic oscillator, substituting the Equation (2.1.1.1) in (2.1.1.3), the number operator $\hat{N}$ takes the form

$$\hat{N} = \frac{1}{\hbar\omega}\left(\frac{\hat{p}^2}{2m} + \frac{1}{2}m\omega^2\hat{q}^2\right) - \frac{\hat{1}}{2} = \frac{1}{\hbar\omega}\hat{H} - \frac{\hat{1}}{2} \tag{2.1.1.5}$$

with an additional term proportional to the system's Hamiltonian operator $\hat{H}$, from which the selfadjointness of $\hat{N}$ can be deduced. This last result is essential for the aim of finding the problem's solution, because it allows the number operator $\hat{N}$ to admit an orthonormal basis of eigenkets $|n\rangle$, that satisfy the eigenvalue equation

$$\hat{N}|n\rangle = |n\rangle n \tag{2.1.1.6}$$

with n only taking non-negative and integral values, the orthonormality relations

$$\langle n'|n\rangle = \delta_{n',n} \tag{2.1.1.7}$$

and the completeness relations

$$\sum_{n=0}^{\infty} |n\rangle\langle n| = \hat{1}. \tag{2.1.1.8}$$

The application of the annihilation and creation operators ($\hat{a}$ and $\hat{a}^\dagger$) on such kets is known under the name of ladder properties

$$\begin{cases} \hat{a}|n\rangle = |n-1\rangle\sqrt{n} \\ \hat{a}^\dagger|n\rangle = |n+1\rangle\sqrt{n+1} \end{cases} \tag{2.1.1.9}$$

which can be used to write an arbitrarily chosen eigenket $|n\rangle$ starting from the ground state $|0\rangle = |n=0\rangle$ as

$$|n\rangle = \hat{a}^{\dagger n}|0\rangle\frac{1}{\sqrt{n!}}. \tag{2.1.1.10}$$

Now, it is possible and convenient to find the alternative expression of the 1D harmonic oscillator's Hamiltonian operator $\hat{H}$ from the Equation (2.1.1.5)

$$\hat{H} = \hbar\omega\left(\hat{N} + \frac{\hat{1}}{2}\right) \tag{2.1.1.11}$$

that clearly shows how the energy eigenvalue problem is solved by the orthonormal basis of eigenket $|n\rangle$ of the number operator $\hat{N}$. Indeed, the kets $|n\rangle$ also satisfy the following eigenvalue equation

$$\hat{H}|n\rangle = |n\rangle u_n, \tag{2.1.1.12}$$

where the energy eigenvalues u_n are given by

$$u_n = \hbar\omega\left(n + \frac{1}{2}\right) \tag{2.1.1.13}$$

and form a completely non-degenerate discrete energy spectrum with a constant gap of $\hbar\omega$ starting from the ground-state level $u_0 = \frac{1}{2}\hbar\omega$.

2.1.2 Statistical description

Once the expression of 1D harmonic oscillator's energy eigenvalues is found and written as in Equation (2.1.1.13), one can move on to a statistical approach in order to calculate some thermodynamic quantities of interest. Therefore, supposing to have a canonical ensemble of such systems, the probability p_j for the j-th energy level u_j is given by

$$p_j = \frac{1}{Z}e^{-\beta u_j} = \frac{1}{Z}e^{-\beta\hbar\omega(j+\frac{1}{2})} \tag{2.1.2.1}$$

with $j \geq 0$ assuming only integral values and Z being the canonical partition function, whose expression reads as

$$\begin{aligned} Z &= \sum_{j=0}^{\infty} e^{-\beta u_j} = \sum_{j=0}^{\infty} e^{-\beta\hbar\omega(j+\frac{1}{2})} = \\ &= e^{-\frac{1}{2}\beta\hbar\omega}\sum_{j=0}^{\infty} e^{-\beta\hbar\omega j} \end{aligned} \tag{2.1.2.2}$$

and reduces to

$$Z = e^{-\frac{1}{2}\beta\hbar\omega}\left(\frac{1}{1-e^{-\beta\hbar\omega}}\right) = \frac{1}{2\sinh(\frac{1}{2}\beta\hbar\omega)} \tag{2.1.2.3}$$

thanks to the convergence of geometric series, which arises from the certain condition

$$e^{-\beta\hbar\omega} < 1. \tag{2.1.2.4}$$

In addition to ensuring the probability normalization, the canonical partition function Z leads to obtain the analytical formulae of physical quantities by relatively simple

mathematical operations. For example, one can get the mean energy U of 1D harmonic oscillators as

$$\begin{aligned} U &= -\frac{1}{Z}\frac{\partial Z}{\partial \beta} = -\frac{\partial}{\partial \beta}\ln Z = \\ &= -\frac{\partial}{\partial \beta}\left[\ln e^{-\frac{1}{2}\beta\hbar\omega} - \ln(1-e^{-\beta\hbar\omega})\right] = \\ &= -\frac{\partial}{\partial \beta}\left[-\frac{1}{2}\beta\hbar\omega - \ln(1-e^{-\beta\hbar\omega})\right] = \\ &= \frac{1}{2}\hbar\omega + \left(\frac{1}{1-e^{-\beta\hbar\omega}}\right)(\hbar\omega e^{-\beta\hbar\omega}) = \\ &= \hbar\omega\left(\frac{1}{2} + \frac{1}{e^{\beta\hbar\omega}-1}\right) = \frac{1}{2}\hbar\omega\coth\left(\frac{1}{2}\beta\hbar\omega\right). \end{aligned} \tag{2.1.2.5}$$

Then, it is also possible to give an alternative physical interpretation to the arbitrary Hamiltonian eigenvalue u_j, which consists in regarding it as the energy required to provide j excitations of quanta $\hbar\omega$ to the 1D harmonic oscillator. Hence the mean number of excitations $\langle n_{\hbar\omega}\rangle$ within the canonical ensemble is found out to be

$$\begin{aligned} \langle n_{\hbar\omega}\rangle = \langle j\rangle &= \sum_{j=0}^{\infty} j p_j = \frac{1}{Z}\sum_{j=0}^{\infty} j e^{-\beta u_j} = \\ &= \frac{1}{Z}\sum_{j=0}^{\infty}\left(j + \frac{1}{2} - \frac{1}{2}\right)e^{-\beta u_j} = \\ &= \frac{1}{Z}\left[\sum_{j=0}^{\infty}\left(j+\frac{1}{2}\right)e^{-\beta u_j} - \frac{1}{2}\sum_{j=0}^{\infty} e^{-\beta u_j}\right] = \\ &= \frac{1}{Z\hbar\omega}\sum_{j=0}^{\infty} u_j e^{-\beta u_j} - \frac{1}{2} = \\ &= \frac{U}{\hbar\omega} - \frac{1}{2} = \frac{1}{e^{\beta\hbar\omega}-1} \end{aligned} \tag{2.1.2.6}$$

using the well-known definition of mean energy, which reads as

$$U = \sum_{j=0}^{\infty} u_j p_j. \tag{2.1.2.7}$$

2.2 The Dulong-Petit law

The Dulong-Petit model is based on the classical harmonic approximation of the interaction potential acting on the N atoms of a lattice. Thus the Hamiltonian of the system

takes the form

$$H = \sum_{i=1}^{N} \frac{p^{(i)2}}{2m_i} + U^{eq} + U^{harm} \tag{2.2.0.1}$$

where $p^{(i)}$ and m_i are respectively the momentum modulus and the mass of the i-th atom, while U^{eq} specifies the equilibrium potential value and U^{harm} is the harmonic term given by

$$U^{harm} = \frac{1}{2} \sum_{j,k}^{N} \vec{u}^{\,(j)}(t) D^{(j,k)}(t) \vec{u}^{\,(k)}(t). \tag{2.2.0.2}$$

The symbol $\vec{u}^{\,(j)}(t)$ stands for the displacement vector of the j-th atom, and $D^{(j,k)}(t)$ instead is a 3×3 square matrix, whose generic (μ, ν)-th element reads as

$$D^{(j,k)}_{\mu,\nu}(t) = \delta_{j,k} \left(\sum_{l}^{N} \phi^{(j,l)}_{\mu,\nu} \right) - \phi^{(j,k)}_{\mu,\nu} \tag{2.2.0.3}$$

where $\delta_{j,k}$ is the Kronecker delta and $\phi^{(j,k)}_{\mu,\nu}$ stands for the Hessian matrix element of the exact interaction potential $\phi^{(j,k)}(r)$ (similar to that of Lennard-Jones) acting between the arbitrarily chosen j-th and k-th ions, which is indicated explicitly by

$$\phi^{(j,k)}_{\mu,\nu} = \frac{\partial^2 \phi^{(j,k)}(r)}{\partial r_\mu \, \partial r_\nu}. \tag{2.2.0.4}$$

So, the internal energy U of the crystal is calculated by the following weighted average among all possible ionic configurations

$$U = \frac{\int d\Gamma e^{-\beta H} H}{\int d\Gamma e^{-\beta H}} = -\frac{\partial}{\partial \beta} \ln \left(\int d\Gamma e^{-\beta H} \right) \tag{2.2.0.5}$$

with $d\Gamma$ as the infinitesimal path in the lattice phase space

$$d\Gamma = \prod_{i=1}^{N} d\vec{u}^{\,(i)} \cdot d\vec{p}^{\,(i)}. \tag{2.2.0.6}$$

If the canonical variables $\vec{u}^{\,(i)}$ and $\vec{p}^{\,(i)}$ are changed to the new ones $\vec{W}^{(i)}$ and $\vec{P}^{(i)}$ via

$$\begin{cases} \vec{u}^{\,(i)} = \beta^{-1/2} \vec{W}^{(i)} \\ \vec{p}^{\,(i)} = \beta^{-1/2} \vec{P}^{(i)} \end{cases} \quad \Rightarrow \quad \begin{cases} d\vec{u}^{\,(i)} = \beta^{-3/2} d\vec{W}^{(i)} \\ d\vec{p}^{\,(i)} = \beta^{-3/2} d\vec{P}^{(i)}, \end{cases} \tag{2.2.0.7}$$

and the expressions of $d\Gamma$ and U^{harm} are substituted into the internal energy formula,

the integral in Equation (2.2.0.5) explicitly reads as

$$\int d\Gamma e^{-\beta H} = e^{-\beta U^{eq}} \beta^{-3N} \left\{ \int \prod_i d\vec{W}^{(i)} \cdot d\vec{P}^{(i)} \exp\left[-\sum_i \frac{\vec{P}^{(i)2}}{2m_i} - \frac{1}{2} \sum_{i,j} \vec{W}^{(i)} D^{(i,j)} \vec{W}^{(j)} \right] \right\}. \tag{2.2.0.8}$$

Being the content of the curly brackets temperature independent, one can finally derive partially with respect to β and thus obtain

$$U = U^{eq} + 3Nk_BT \tag{2.2.0.9}$$

from which the heat capacity c can be calculated as

$$c = \frac{\partial U}{\partial T} = 3Nk_B. \tag{2.2.0.10}$$

This result is known as the Dulong-Petit law, that turns out to be not consistent with the experimental data for real solids. Indeed, in the low temperature limit the effective heat capacity rapidly decreases until it completely vanishes, while in the high temperature case it grows continuously to an horizontal asymptote which is nevertheless not the same as the Dulong-Petit expected value. The main reason for this last incompatibility consists in the arising of significant anharmonic terms in the interaction potential as the temperature increases.

2.3 The Einstein model

The Einstein model for the characterization of phononic properties of materials is essentially based on the assumption that all $3N$ vibrational modes of the crystal lattice can be approximated to 1D simple harmonic oscillators with same frequency ω_E. This directly implies a Dirac delta shaped distribution of the frequencies among the normal modes, which may seem an unrealistic hypothesis, but actually its analytical results show good compatibility with experimental data in some particular cases, as explained in Section 2.5.

Further assuming the independence of normal modes, the total partition function Z can be written as

$$Z = \prod_{k=1}^{3N} Z_k \tag{2.3.0.1}$$

where the generic factor Z_k is the partition function of the k-th mode that in harmonic approximation takes the form

$$Z_k = \frac{e^{-\frac{1}{2}\beta\hbar\omega_E}}{1 - e^{-\beta\hbar\omega_E}}. \tag{2.3.0.2}$$

Due to the initial assumption of the Einstein model, Z_k clearly does not depend on the index k. As a consequence, the product in Equation (2.3.0.1) reduces to

$$Z = (Z_k)^{3N} \tag{2.3.0.3}$$

and its natural logarithm instead becomes

$$\begin{aligned} \ln(Z) &= \ln(Z_k)^{3N} = 3N \ln(Z_k) = \\ &= 3N \left[\ln(e^{-\frac{1}{2}\beta\hbar\omega_E}) - \ln(1 - e^{-\beta\hbar\omega_E}) \right] = \\ &= 3N \left[-\frac{1}{2}\beta\hbar\omega_E - \ln(1 - e^{-\beta\hbar\omega_E}) \right]. \end{aligned} \tag{2.3.0.4}$$

Now, the internal energy U can be found as the following partial derivative with respect to the variable β

$$\begin{aligned} U &= -\frac{\partial}{\partial\beta} \ln(Z) = -3N \frac{\partial}{\partial\beta} \left[-\frac{1}{2}\beta\hbar\omega_E - \ln(1 - e^{-\beta\hbar\omega_E}) \right] = \\ &= \frac{3}{2} N\hbar\omega_E + \left(\frac{3N}{1 - e^{-\beta\hbar\omega_E}} \right) (\hbar\omega_E e^{-\beta\hbar\omega_E}) = \\ &= 3N\hbar\omega_E \left(\frac{1}{2} + \frac{1}{e^{\beta\hbar\omega_E} - 1} \right) \end{aligned} \tag{2.3.0.5}$$

that could also be obtained by multiplying the mean energy of a 1D harmonic oscillator of frequency ω_E by the total number $3N$ of normal modes. It turns out to be useful to define a parameter T_E, known as Einstein temperature and given by

$$T_E = \frac{\hbar\omega_E}{k_B}, \tag{2.3.0.6}$$

in terms of which the internal energy U can be expressed as

$$\begin{aligned} U &= 3Nk_B T_E \left(\frac{1}{2} + \frac{1}{e^{\beta k_B T_E} - 1} \right) = \\ &= 3Nk_B T_E \left(\frac{1}{2} + \frac{1}{e^{T_E/T} - 1} \right). \end{aligned} \tag{2.3.0.7}$$

Finally, one can proceed to calculate the heat capacity c (because of the validity of $c \equiv c_p \simeq c_v$ for solids with the heat capacities c_p at constant pressure and c_v at constant volume) as follows

$$c = \frac{\partial U}{\partial T} = -\frac{3Nk_B T_E}{(e^{T_E/T} - 1)^2} \left(-\frac{T_E}{T^2} e^{T_E/T} \right) = 3Nk_B \frac{x^2 e^x}{(e^x - 1)^2} \tag{2.3.0.8}$$

introducing the new variable $x = \frac{T_E}{T}$.
As shown in Figure 2.3, in the low temperature limit for $T \to 0$ and consequently $x \to +\infty$ it exhibits a rapidly vanishing trend of the form

$$c = 3Nk_B \frac{x^2 e^x}{e^{2x}(1 - e^{-x})^2} \to 3Nk_B x^2 e^{-x} \tag{2.3.0.9}$$

because of the dominant factor $e^{-x} = e^{-T_E/T}$, while in the high temperature limit for $T \to +\infty$ and $x \to 0$ it becomes practically constant

$$\begin{aligned} c &= 3Nk_B \frac{x^2(1 + x + x^2/2 + o(1))}{(1 + 2x + (2x)^2/2 + o(1) - 2(1 + x + x^2/2 + o(1)) + 1)} = \\ &= 3Nk_B \frac{x^2(1 + x + x^2/2 + o(1))}{x^2(1 + o(1))} \to 3Nk_B \end{aligned} \tag{2.3.0.10}$$

in full agreement with the classical Dulong-Petit law in Equation (2.2.0.10) and the energy equipartition theorem.

2.4 The Debye model

As an improvement of the Einstein model, the Debye model for phonons in a crystal lattice assumes a more generic form of frequencies distribution among the normal modes, which takes the name of the density of vibrational states $g(\omega)$ and differs from the previous Dirac delta shaped one

$$g_E(\omega) = 3N\delta(\omega - \omega_E) \tag{2.4.0.1}$$

represented in Figure 2.1.

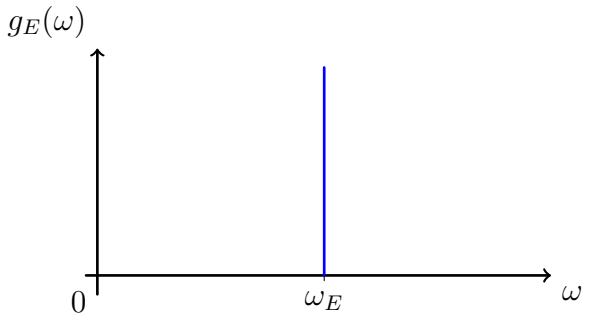

Figure 2.1: *The Dirac delta shaped density of vibrational states expected by the Einstein model.*

In particular, such a function $g(\omega)$, as well as $g_E(\omega)$, must satisfy the following normalization condition

$$\int_0^\infty g(\omega)d\omega = 3N \tag{2.4.0.2}$$

being $3N$ the total number of vibrational modes of the crystal lattice.
Now, in order to find an analytical expression of $g(\omega)$, two important assumptions concerning the phonons' propagation are taken into account. The first states that their speed is constant in time, uniform in all normal modes and equal to the specific sound velocity of the material v_s. The second one consists in supposing the linearity of the dispersion relation

$$\omega = v_s q \tag{2.4.0.3}$$

with $q = |\vec{q}|$ being the phonon wave vector modulus.
This last hypothesis turns out to be valid in the low temperature limit, but not in the high one due to the arising of potential anharmonicity.
Proceeding to the determination of $g(\omega)$, the number of vibrational states included in the spherical crown of infinitesimal thickness dq in the reciprocal space can be calculated by the quantity

$$g(q)dq = \frac{4\pi q^2 dq}{(\frac{2\pi}{L})^3} \times 3, \tag{2.4.0.4}$$

where the factor 3 results from the three possible phonon polarizations, and $\left(\frac{2\pi}{L}\right)^3$ in the denominator is the elementary cubic volume in the reciprocal space, that is indeed quantized due to the spatial confinement of phonons in a cubic crystal lattice of side L. Then, substituting the linear dispersion relation in Equation (2.4.0.3) into (2.4.0.4), the analytical expression of the density of vibrational states $g(\omega)$ is finally obtained as

$$g(\omega) = \frac{3V\omega^2}{2\pi^2 v_s^3} \tag{2.4.0.5}$$

with the cubic volume $V = L^3$. In Figure 2.2, the final trend of $g(\omega)$ is shown.
However, it is further assumed that exists a maximum frequency ω_D, called Debye frequency, at which atoms can vibrate around their equilibrium position. This implies that the normalization condition in Equation (2.4.0.2) undergoes the following simplification

$$\int_0^{\omega_D} g(\omega)d\omega = 3N \tag{2.4.0.6}$$

from which an analytical expression for ω_D can be easily found by substituting the formula in Equation (2.4.0.5) into (2.4.0.6) as follows

$$\frac{3V}{2\pi^2 v_s^3}\int_0^{\omega_D} \omega^2 d\omega = \frac{V\omega_D}{2\pi^2 v_s^3} = 3N \quad \Rightarrow \quad \omega_D = (6\pi^2 v_s^3 n)^{1/3} \tag{2.4.0.7}$$

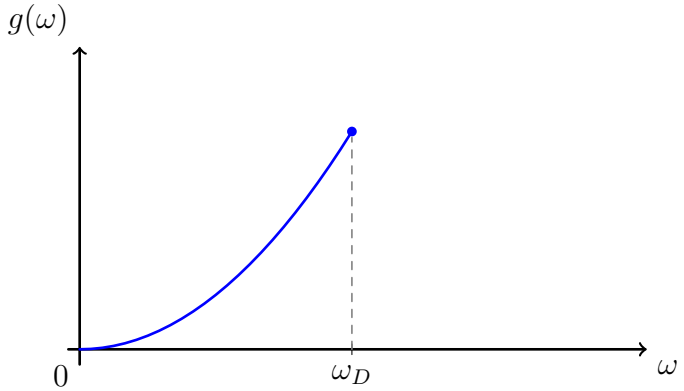

Figure 2.2: *The density of vibrational states expected by the Debye model.*

with the volumetric density of atoms in the crystal lattice $n = \frac{N}{V}$.
The so calculated Debye frequency ω_D thus depends on the material specific quantities n and v_s. Moreover, it allows not only to rewrite the density of vibrational states as

$$g(\omega) = \frac{9N}{\omega_D^3}\omega^2, \tag{2.4.0.8}$$

but also to define the Debye temperature

$$T_D = \frac{\hbar\omega_D}{k_B} \tag{2.4.0.9}$$

that takes the typical values in Table 2.1.

Material	Debye temperature (K)
Ne	63
Na	150
NaCl	321
Al	394
Si	625
C (diamond)	1860

Table 2.1: *Table of experimental estimates of Debye temperature for some exemplary materials from* [4].

Once $g(\omega)$ is fully determined, one can move on to find the internal energy U expected by the Debye model via the following integration

$$U = \int_0^{\omega_D} g(\omega)\hbar\omega\langle n_{\hbar\omega}\rangle d\omega = \frac{9N\hbar}{\omega_D^3}\int_0^{\omega_D} \frac{\omega^3}{e^{\beta\hbar\omega}-1}d\omega \tag{2.4.0.10}$$

that can be solved by changing variable to the dimensionless

$$x = \frac{\hbar\omega}{k_B T} \quad \Rightarrow \quad x_D = \frac{\hbar\omega_D}{k_B T} = \frac{T_D}{T}. \tag{2.4.0.11}$$

So, the expression for U in Equation (2.4.0.10) becomes

$$\begin{aligned} U &= \frac{9N\hbar}{\omega_D^3}\left(\frac{k_B T}{\hbar}\right)^4 \int_0^{x_D} \frac{x^3}{e^x - 1} dx = \\ &= 9Nk_B T \left(\frac{T}{T_D}\right)^3 \int_0^{T_D/T} \frac{x^3}{e^x - 1} dx \end{aligned} \tag{2.4.0.12}$$

and the integral admits an already known solution when the condition $T \ll T_D$ holds. Such a solution is given by the product $\Gamma(4)\zeta(4) = \frac{6\pi^4}{90}$ of the Euler gamma and Riemann zeta functions, respectively indicated by $\Gamma(z)$ and $\zeta(s)$ and defined as

$$\begin{cases} \Gamma(z) = \int_0^\infty t^{z-1} e^{-t} dt \\ \zeta(s) = \sum_{n=1}^\infty \frac{1}{n^s}. \end{cases} \tag{2.4.0.13}$$

Therefore, the internal energy U in the low temperature limit reads as

$$U = \frac{3\pi^4 N k_B}{5T_D^3} T^4 \tag{2.4.0.14}$$

and consequently the heat capacity c is derived as

$$c = \frac{\partial U}{\partial T} = \frac{12\pi^4 N k_B}{5T_D^3} T^3 \tag{2.4.0.15}$$

which is known as the Debye T^3 law. This last result turns out to represent correctly the low temperature heat capacity trend of many materials.
In the high temperature limit for $T \gg T_D$, instead, the integrand function can be approximated to its behaviour for $x \to 0$

$$\int_0^{T_D/T} \frac{x^3}{e^x - 1} dx \simeq \int_0^{T_D/T} x^2 dx = \frac{1}{3}\left(\frac{T_D}{T}\right)^3. \tag{2.4.0.16}$$

As a consequence, the internal energy U in this case becomes

$$U = 3Nk_B T, \tag{2.4.0.17}$$

while the heat capacity c

$$c = \frac{\partial U}{\partial T} = 3Nk_B \tag{2.4.0.18}$$

in conformity with the Dulong-Petit law and the energy equipartition theorem.
In order to find a heat capacity function valid for the whole temperature range $[0, +\infty]$, it is possible to derive partially the internal energy U written in Equation (2.4.0.10) with respect to the temperature T as follows

$$\begin{aligned} c = \frac{\partial U}{\partial T} &= \frac{9N\hbar}{\omega_D^3} \int_0^{\omega_D} \frac{-\omega^3}{(e^{\beta\hbar\omega} - 1)^2} \left(-\frac{\hbar\omega}{k_B T^2} e^{\beta\hbar\omega} \right) d\omega = \\ &= \frac{9N\hbar}{T\omega_D^3} \left(\frac{k_B T}{\hbar} \right)^4 \int_0^{x_D} \frac{x^4 e^x}{(e^x - 1)^2} dx = \\ &= \frac{9Nk_B}{x_D^3} \int_0^{x_D} \frac{x^4 e^x}{(e^x - 1)^2} dx. \end{aligned} \tag{2.4.0.19}$$

The whole heat capacity trend expected by the Debye model is plotted in Figure 2.3 thanks to numerical integration of Equation (2.4.0.19), and it is also overlapped with the Einstein result of Equation (2.3.0.8) in the particular condition $T_E = T_D$. The graph clearly shows how in the high temperature limit both functions grow asymptotically to $C = {}^{c}/_{n} \to 3R$, but also that the low temperature trend predicted by the Einstein model ($\propto \frac{1}{T^2} e^{-1/T}$) vanishes way more rapidly than the Debye one ($\propto T^3$).

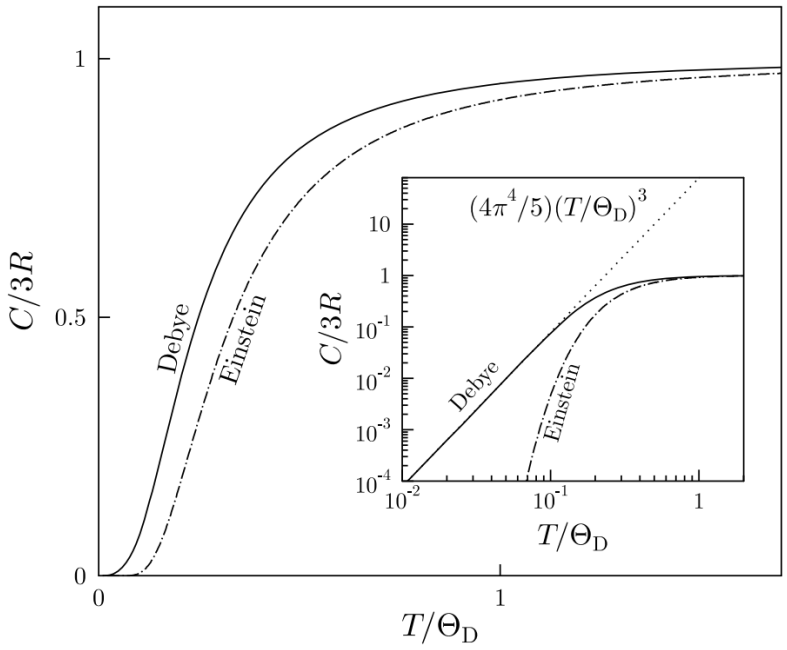

Figure 2.3: *Graph of the Einstein and Debye molar heat capacities as functions of temperature T, which is normalized by the Debye temperature T_D, here indicated by Θ_D. To further emphasize the difference between the two results, a log-log scale plot is inserted.*

In addition, the experimental temperature dependence of heat capacity evidences high compatibility to the Debye estimate, which is mainly due to three reasons. The first is the precision of the total number of normal modes; the second consists in the absence of phase transitions between the low and high temperature limits; the third is the accuracy of the Bose-Einstein distribution, which decreases rapidly with the frequency ω.

2.5 Phononic dispersion

In this section, some exemplary models of phononic dispersion in both 1D and 3D lattices are discussed. The aim is simply to understand in a more practical way how the assumptions of the Debye model about the linear dispersion relation in Equation (2.4.0.3) become untruthful.
For example, in general the propagation velocity v_s is not constant and uniform among all the normal modes, but instead takes different values $v_{s,T}$ and $v_{s,L}$ according to their transverse or longitudinal nature. Hence a better estimate of the sound velocity v_s of the material can be obtained by

$$\frac{3}{v_s^3} = \frac{2}{v_{s,T}^3} + \frac{1}{v_{s,L}^3} \tag{2.5.0.1}$$

with weights equal to the associated number of modes per atom.
First of all, the amplitude of oscillations will be considered small with respect to the atomic distances. So, the interaction potential acting on neighbouring ions will be reasonably approximated to be harmonic.
Moreover, the next models for crystal lattices of a finite number N of atoms necessarily need the definition of the atomic interaction at the boundaries, and in mathematical terms this implies a significant complication. In order to avoid it and to seek simplicity as much as possible, the Born-von Karman periodic boundary conditions will be applied to the atomic displacement functions.
For 1D chains, the displacement u_n must satisfy

$$\begin{cases} u_{N+1} = u_1 \\ u_0 = u_N, \end{cases} \tag{2.5.0.2}$$

while for 3D Bravais lattices such functions will be indicated by $\vec{u}^{\,(j)}(t)$ and obey the following rule

$$\vec{u}^{\,(k)}(t) = \vec{u}^{\,(j)}(t) \quad \forall k \in \mathbb{N} \quad | \quad \vec{R}^{(k)} = \vec{R}^{(j)} + N_\mu \vec{a}_\mu \tag{2.5.0.3}$$

where $\mu = 1, 2, 3$ are the only allowed index values, N_1, N_2, N_3 are integers such that $N_1 N_2 N_3 = N$ and $\vec{a}_1$, $\vec{a}_2$, $\vec{a}_3$ are the later defined lattice vectors.
At last, two possible kinds of phononic dispersion curves can be observed.

The first is usually called acoustic branch, due to the coincidence of the group velocity $v_g = \frac{d\omega}{dq}$ with the sound speed v_s for $|\vec{q}| \to 0$. In addition, in that limit the curve tends to 0 and the atoms vibrate almost in phase. The associated normal modes go under the name of acoustic modes and they are well described by the Debye model because at low temperatures, and thus frequencies, the dispersion relation of real solids is approximately linear.
The second instead is called optic branch. For $|\vec{q}| \to 0$, it exhibits a non-vanishing value and involves atomic vibrations almost out of phase, which are the typical motions of ions in a lattice subjected to an external electromagnetic radiation. In this case, the related normal modes are known as optic modes and their behaviour is very similar to that expected by the Einstein model because of the near-constancy of the frequency with respect to $\vec{q}$.

2.5.1 1D monoatomic linear chain

Consider a 1D linear chain of N atoms of mass m, equally spaced by the lattice step a and interacting with the neighbours via springs of elastic constant k, as summarized in Figure 2.4.

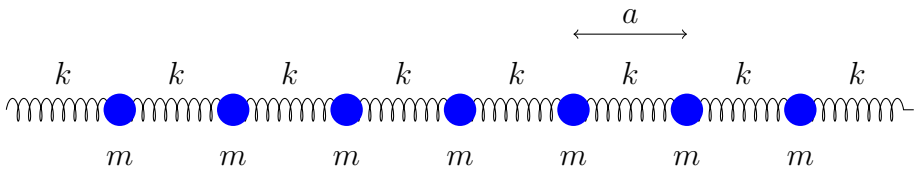

Figure 2.4: *Pictorial representation of a 1D monoatomic linear chain.*

The equation of motion for the n-th atom is given by

$$\begin{aligned} m\ddot{u}_n &= k(u_{n+1} - u_n) - k(u_n - u_{n-1}) = \\ &= k(u_{n+1} - 2u_n + u_{n-1}) \end{aligned} \tag{2.5.1.1}$$

where the variable u_n indicates the displacement of the n-th atom from its equilibrium position.
Since the purpose of the topic is to find the frequencies ω of collective oscillations of the crystal lattice, one can look for a plane and harmonic wave solution of the form

$$u_n = u\ e^{i(qna - \omega t)} \tag{2.5.1.2}$$

with u and q respectively the amplitude and the wave number of such a motion. This displacement function must satisfy the 1D Born-von Karman periodic boundary conditions in Equation (2.5.0.2), which in fact is equivalent to require a quantization of the reciprocal space as

$$e^{iqNa} = 1 \quad \Rightarrow \quad q = \frac{2\pi}{aN} j \quad j \in \mathbb{Z}. \tag{2.5.1.3}$$

Then, the substitution of Equation (2.5.1.2) into (2.5.1.1) brings out

$$m\omega^2 = -k(e^{iqa} - 2 + e^{-iqa}) = 2k(1 - \cos(qa)) = 4k\sin^2\left(\frac{qa}{2}\right) \tag{2.5.1.4}$$

and allows to obtain the aimed dispersion relation as

$$\omega(q) = \sqrt{\frac{4k}{m}}\left|\sin\left(\frac{qa}{2}\right)\right| \tag{2.5.1.5}$$

which is plotted in Figure 2.5 exclusively for the first Brillouin zone $[-\frac{\pi}{a}, \frac{\pi}{a}]$.

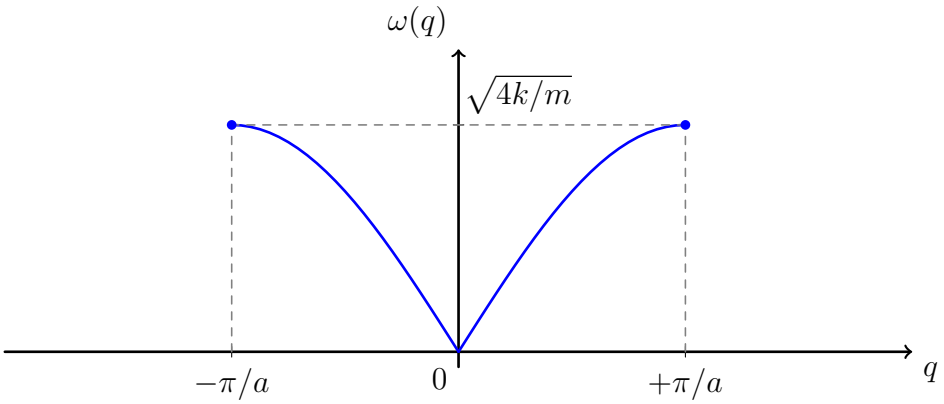

Figure 2.5: *The phonon dispersion relation for a 1D monoatomic linear chain.*

In the high wavelength limit for $q = \frac{2\pi}{\lambda} \to 0$, the dispersion relation $\omega(q)$ becomes linear

$$\omega(q) \to v_s|q| \tag{2.5.1.6}$$

with the proportionality coefficient $v_s = a\sqrt{\frac{k}{m}}$ as the material sound velocity.
Only in this precise case, the linear approximation of the dispersion relation assumed by the Debye model turns out to be valid for the 1D monoatomic linear chain system.

2.5.2 1D diatomic linear chain

Consider now a 1D linear chain of two alternating atoms of different masses M_1, M_2 and connected by springs of elastic constant k. The average distance between neighbouring atoms is indicated by a, hence the lattice spacing is easily given by $a' = 2a$.
The system is illustrated in Figure 2.6.

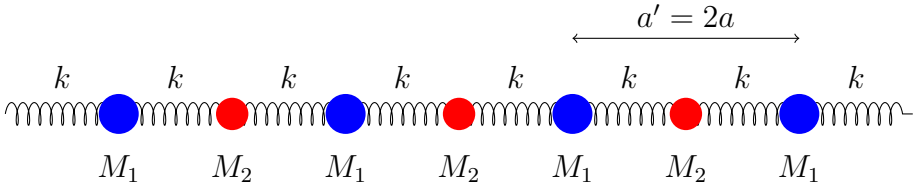

Figure 2.6: *Pictorial representation of a 1D diatomic linear chain.*

The equations of motion for the atoms in the n-th pair actually are very similar to that of Equation (2.5.1.1) for the 1D monoatomic linear chain and they read as

$$\begin{cases} M_1 \ddot{u}_n = k(v_n - 2u_n + v_{n-1}) \\ M_2 \ddot{v}_n = k(u_{n+1} - 2v_n + u_n) \end{cases} \tag{2.5.2.1}$$

where the variables u_n and v_n are respectively the displacements of the first and second atom in the n-th pair from their equilibrium position.
Again the solutions of the Equations (2.5.2.1) are required to take the form of plane and harmonic waves

$$\begin{cases} u_n = u\ e^{i(qna' - \omega t)} \\ v_n = v\ e^{i(qna' - \omega t)} \end{cases} \tag{2.5.2.2}$$

with u and v amplitudes, q wave number and ω frequency of the collective oscillations. These two guess functions must obey 1D Born-von Karman periodic boundary conditions, that imply a reciprocal space quantization practically identical to the 1D monoatomic linear chain case.
Then, substituting the Equations (2.5.2.2) into (2.5.2.1), the second ones undergo the following modifications

$$\begin{cases} M_1 u\omega^2 = -k[v(e^{-iqa'} + 1) - 2u] \\ M_2 v\omega^2 = -k[u(e^{iqa'} + 1) - 2v] \end{cases} \tag{2.5.2.3}$$

and thus organize in the homogeneous linear system

$$\begin{cases} (2k - M_1\omega^2)u - k(e^{-iqa'} + 1)v = 0 \\ (2k - M_2\omega^2)v - k(e^{iqa'} + 1)u = 0. \end{cases} \tag{2.5.2.4}$$

Such a system of Equations (2.5.2.4) admit solutions only if the following condition is fulfilled

$$\det \begin{pmatrix} 2k - M_1\omega^2 & -k(e^{-iqa'} + 1) \\ -k(e^{iqa'} + 1) & 2k - M_2\omega^2 \end{pmatrix} = 0 \tag{2.5.2.5}$$

that is equivalent to

$$\begin{aligned} &4k^2 - 2k\omega^2(M_1 + M_2) + M_1M_2\omega^4 - k^2(e^{2iqa} + 1)(e^{-2iqa} + 1) = 0 \\ &M_1M_2\omega^4 - 2k\omega^2(M_1 + M_2) + 2k^2(1 - \cos(2qa)) = 0 \\ &\omega^4 - 2k\omega^2\left(\frac{1}{M_1} + \frac{1}{M_2}\right) + \frac{4k^2}{M_1M_2}\sin^2(qa) = 0 \end{aligned} \tag{2.5.2.6}$$

from which the square of the two possible solutions $\omega_\pm(q)$ is derived as

$$\omega_\pm^2(q) = k\left(\frac{1}{M_1} + \frac{1}{M_2}\right) \pm \sqrt{k^2\left(\frac{1}{M_1} + \frac{1}{M_2}\right)^2 - \frac{4k^2}{M_1M_2}\sin^2(qa)}. \tag{2.5.2.7}$$

The phonon dispersion relation for a 1D diatomic linear chain thus exhibits two branches as shown in Figure 2.7.

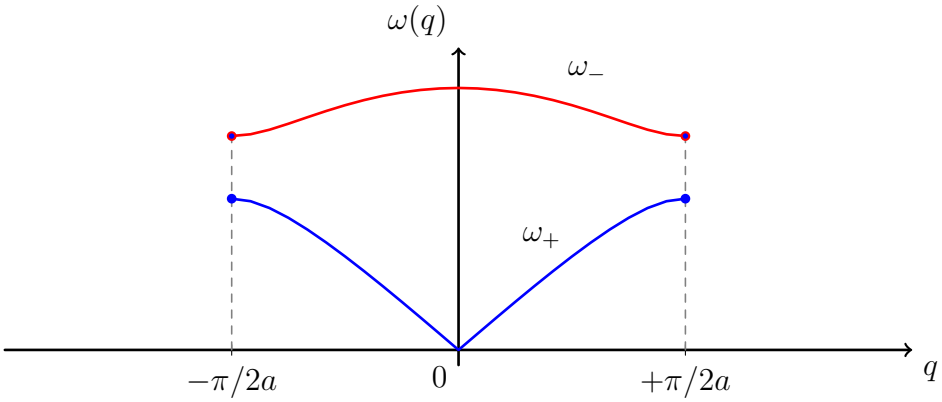

Figure 2.7: *The phonon dispersion curves for a 1D diatomic linear chain: optic branch* $\omega_+(q)$ *in red and acoustic branch* $\omega_-(q)$ *in blue.*

The first $\omega_+(q)$ is called optic branch and it is mainly characterized by the non-vanishing frequency that reaches for $q = 0$ and is equal to

$$\omega_+(q = 0) = \sqrt{2k\left(\frac{1}{M_1} + \frac{1}{M_2}\right)}. \tag{2.5.2.8}$$

Instead the second one $\omega_-(q)$ is known as acoustic branch and it behaves very similiarly to the 1D monoatomic linear chain dispersion relation. Indeed, this vanishes for $q = 0$ and reduces to Equation (2.5.1.5) in fulfillment of the condition $M_1 = M_2 \equiv m$ as

$$\begin{aligned} \omega_-^2(q) &= \frac{2k}{m} - \sqrt{\frac{4k^2}{m^2} - \frac{4k^2}{m^2}\sin^2(qa)} = \frac{2k}{m}\left(1 - \sqrt{1 - \sin^2(qa)}\right) = \\ &= \frac{2k}{m}(1 - \cos(qa)) = \frac{4k}{m}\sin^2\left(\frac{qa}{2}\right). \end{aligned} \tag{2.5.2.9}$$

This is in fact the simplest model of phononic dispersion, where an optic branch can be observed.

2.5.3 3D monoatomic Bravais lattice

In case of a 3D Bravais lattice of N atoms of mass m, the equilibrium position of the j-th atom with $1 \leq j \leq N$ is given by

$$\vec{R}^{(j)} = n_1^{(j)}\vec{a}_1 + n_2^{(j)}\vec{a}_2 + n_3^{(j)}\vec{a}_3 \tag{2.5.3.1}$$

where $\vec{a}_1$, $\vec{a}_2$ and $\vec{a}_3$ are the lattice vectors, which specify the 3D directions that characterize the crystal translational symmetries, while $n_1^{(j)}$, $n_2^{(j)}$ and $n_3^{(j)}$ are the integral coefficients that univocally determine how many lattice vectors the j-th atom needs to be connected to the origin of axes (must coincide with one of the sites). For a better comprehension an exemplary system is illustrated in Figure 2.8.

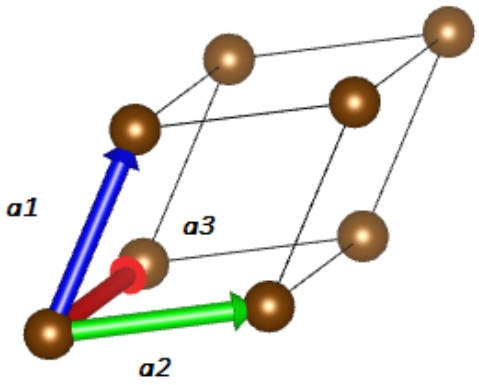

Figure 2.8: *Example of a cubic 3D monoatomic Bravais lattice with marked lattice vectors $\vec{a}_1$ (blue), $\vec{a}_2$ (green) and $\vec{a}_3$ (red).*

Hence the displacement of that atom from $\vec{R}^{(j)}$ at time t is defined as

$$\vec{u}^{\,(j)}(t) = \vec{r}^{\,(j)}(t) - \vec{R}^{(j)} \tag{2.5.3.2}$$

with its effective position $\vec{r}^{\,(j)}(t)$.

The $3N$ equations of motion associated with each component of all N atomic displacement vectors are written in vector notation as

$$m\ddot{\vec{u}}^{\,(j)}(t) = -\frac{\partial U^{harm}}{\partial \vec{u}^{\,(j)}} = -\sum_{k}^{N} D^{(j,k)}(t)\vec{u}^{\,(k)}(t) \tag{2.5.3.3}$$

with the harmonic potential U^{harm} defined in Equation (2.2.0.2) and, as well as in Sections 2.5.1 - 2.5.2, they admit plane and harmonic wave solutions that in this case must be vectors of the form

$$\vec{u}^{\,(j)}(t) = u\hat{\varepsilon}\; e^{i(\vec{q}\cdot\vec{R}^{(j)}-\omega t)} \tag{2.5.3.4}$$

with the unit vector of polarization $\hat{\varepsilon}$, the wave vector $\vec{q}$ and the frequency ω. The application of the 3D Born-von Karman periodic boundary conditions in Equation (2.5.0.3) to this case necessarily lead to a 3D quantization of the reciprocal space, in which the only allowed $\vec{q}$ points are

$$\vec{q} = \frac{n_1}{N_1}\vec{b}_1 + \frac{n_2}{N_2}\vec{b}_2 + \frac{n_3}{N_3}\vec{b}_3 \tag{2.5.3.5}$$

where n_1, n_2, n_3 are integers, while $\vec{b}_1$, $\vec{b}_2$, $\vec{b}_3$ are known as reciprocal lattice vectors and they satisfy the following orthogonality relations

$$\vec{b}_\mu \cdot \vec{a}_\nu = 2\pi\delta_{\mu,\nu} \qquad \mu,\nu = 1,2,3 \tag{2.5.3.6}$$

with the lattice vectors $\vec{a}_1$, $\vec{a}_2$, $\vec{a}_3$.
Once the functions in Equation (2.5.3.4) are substituted into (2.5.3.3), the equations of motion become

$$\begin{aligned} m\omega^2\hat{\varepsilon}\; e^{i(\vec{q}\cdot\vec{R}^{(j)}-\omega t)} &= \sum_{k}^{N} D^{(j,k)}(t)\hat{\varepsilon}\; e^{i(\vec{q}\cdot\vec{R}^{(k)}-\omega t)} \\ m\omega^2\hat{\varepsilon} &= \left(\sum_{k}^{N} D^{(j,k)}(t)\; e^{-i\vec{q}\cdot(\vec{R}^{(j)}-\vec{R}^{(k)})}\right)\hat{\varepsilon} \end{aligned} \tag{2.5.3.7}$$

from which the dynamical matrix $\Delta^{(j)}(\vec{q})$ gets its definition as

$$\Delta^{(j)}(\vec{q}) = \sum_{k}^{N} D^{(j,k)}(t)\; e^{-i\vec{q}\cdot(\vec{R}^{(j)}-\vec{R}^{(k)})} \tag{2.5.3.8}$$

and Equation (2.5.3.3) further reduces to

$$m\omega^2\hat{\varepsilon} = \Delta^{(j)}(\vec{q})\;\hat{\varepsilon}. \tag{2.5.3.9}$$

The 3×3 square matrix $\Delta^{(j)}(\vec{q})$ turns out to be both real and symmetric. This means that for spectral theorem it admits three real eigenvectors $\vec{\varepsilon}_1(\vec{q})$, $\vec{\varepsilon}_2(\vec{q})$, $\vec{\varepsilon}_3(\vec{q})$ which satisfy orthonormality relations

$$\vec{\varepsilon}_s(\vec{q}) \cdot \vec{\varepsilon}_{s'}(\vec{q}) = \delta_{s,s'} \qquad s,s' = 1,2,3 \tag{2.5.3.10}$$

and eigenvalue equations

$$\Delta^{(j)}(\vec{q})\ \vec{\varepsilon}_s(\vec{q}) = \lambda_s(\vec{q})\ \vec{\varepsilon}_s(\vec{q}). \tag{2.5.3.11}$$

The aimed dispersion relation can be finally derived from the real eigenvalues $\lambda_s(\vec{q})$ of the dynamical matrix $\Delta^{(j)}(\vec{q})$ as

$$\omega_s(\vec{q}) = \sqrt{\frac{\lambda_s(\vec{q})}{m}} \tag{2.5.3.12}$$

that clearly depends on the index s. Hence it exhibits three branches, which are proven to be acoustic, since they vanish for $|\vec{q}| = 0$ as shown in Figure 2.9.

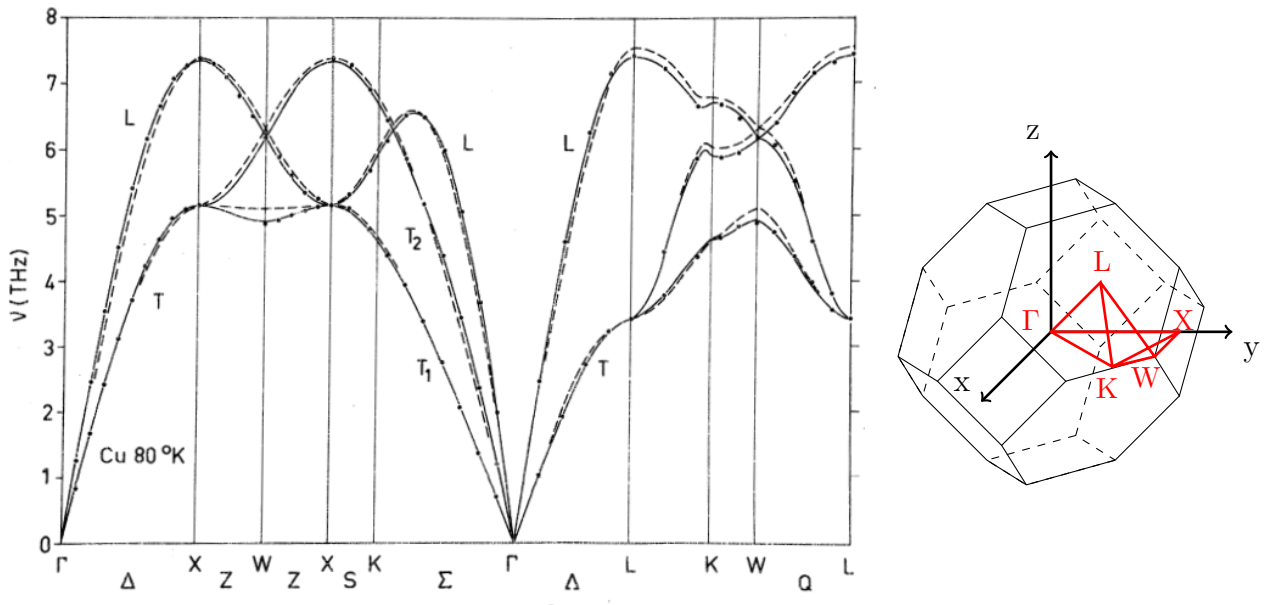

Figure 2.9: *Phononic dispersion relation (left) for a fcc monoatomic lattice of copper Cu at 80K* [13] *and high symmetry paths (red) within the first Brillouin zone (right). Experimental points (dots) are overlapped to two different theoretical results (dashed and solid lines).*

Depending on the lattice 3D structure and its symmetries, the matrix $D^{(j,k)}(t)$ defined in Equation (2.2.0.3) obeys precise relations that correspond to properties for the dynamical matrix $\Delta^{(j)}(\vec{q})$, of which the eigenvalues problem has just been studied. In this way, the symmetries indirectly affect the phononic dispersion relation by identifying particular high symmetry paths within the first Brillouin zone. Along such lines the polarization vectors are well determined and thus allow the distinction between longitudinal and transverse normal modes.
So the dispersion curves $\omega_s(\vec{q})$ are always calculated in those paths and occasionally show phenomena of branches degeneration.

2.5.4 3D Bravais lattice with basis

As in Section 2.5.2, the introduction of a poliatomic basis in the unit cell leads to the occurrence of optic branches in the phononic dispersion relation of the material under study.
In particular, if p is the integral number of ions in the basis, then there will be $3p$ normal modes with associated frequency $\omega_s(\vec{q})$ and $s \in \{1, 2, ..., 3p\}$. It can be demonstrated that only three of those branches turn out to be acoustic, while the other $3(p-1)$ are optic. An example of the resultant dispersion curves is illustrated in Figure 2.10.

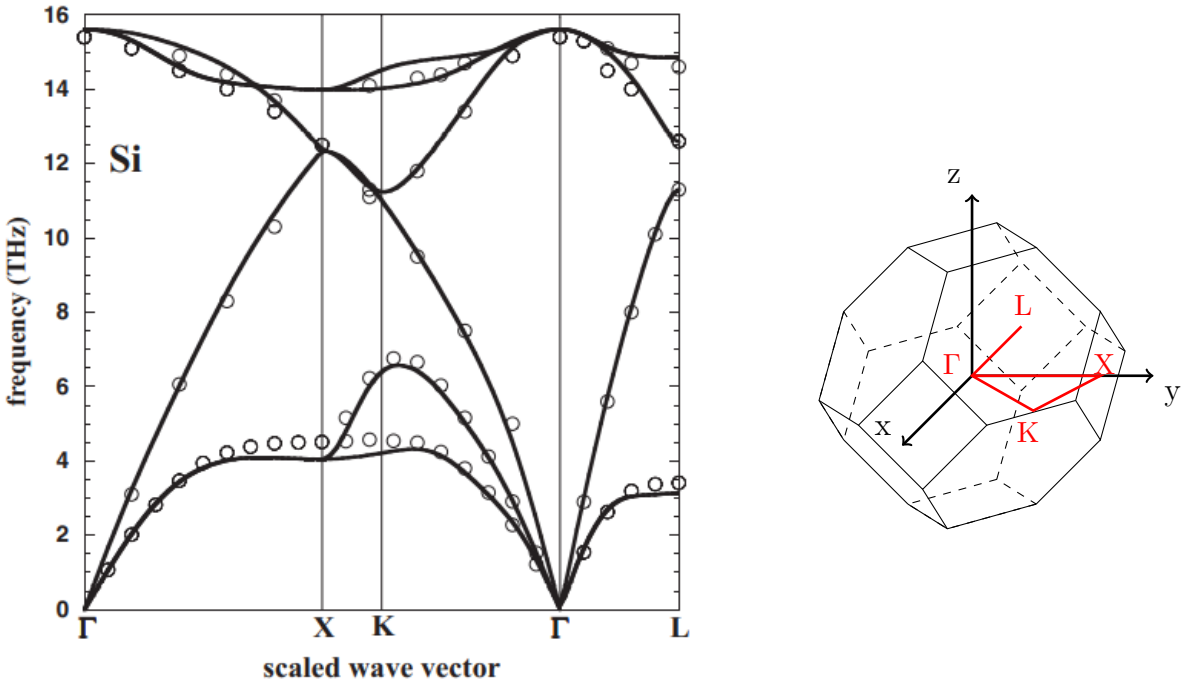

Figure 2.10: *Phononic dispersion relation (left) for a fcc lattice of silicon Si* [14] *with a diatomic basis and high symmetry paths (red) within the first Brillouin zone (right). Experimental points (dots) are overlapped to ab initio calculated frequencies (lines).*

This increases substantially the complexity of finding the analytical solution to the problem. Indeed, for example, the displacement from the equilibrium position of the j-th atom (with $1 \leq j \leq p$) in the l-th basis in the s-th normal mode (with $1 \leq s \leq 3p$) is of the form

$$\vec{u}^{\,(j,l)}(t) = \Re[u_s \vec{\varepsilon}\, e^{i(\vec{q}\cdot\vec{R}^{(j,l)} - \omega t)}], \tag{2.5.4.1}$$

and must solve the equation of motion

$$M_j \ddot{\vec{u}}^{\,(j,l)}(t) = -\sum_{k,l'} D^{(j,l,k,l')}(t)\vec{u}^{\,(k,l')}(t) \tag{2.5.4.2}$$

that leads to the definition of the dynamical matrix in this case as

$$\Delta^{(j,k)}(\vec{q}) = (M_j M_k)^{-1/2} \sum_{l'} D^{(j,0,k,l')}(t) e^{i\vec{q}\cdot(\vec{R}^{(k,l')} - \vec{R}^{(j,0)})} \tag{2.5.4.3}$$

with M_j as the mass of the j-th atom in the basis.
So, the eigenvalue equation for the dispersion curve $\omega_s(\vec{q})$ of the s-th normal mode reads as

$$\sum_k \Delta^{(j,k)}(\vec{q}) \vec{\varepsilon}_s{}^{(k,0)}(\vec{q}) = \omega_s^2(\vec{q}) \vec{\varepsilon}_s{}^{(j,0)}(\vec{q}) \tag{2.5.4.4}$$

with the polarization eigenvectors $\vec{\varepsilon}_s{}^{(j,0)}(\vec{q})$ that must satisfy the following generalized orthogonality relations

$$\sum_{j=1}^{p} \vec{\varepsilon}_s{}^{(j,0)*}(\vec{q}) \cdot \vec{\varepsilon}_{s'}{}^{(j,0)}(\vec{q}) M_j = \delta_{s,s'}. \tag{2.5.4.5}$$

This clearly shows how the procedure actually is the same of Section 2.5.3, but with an inevitably more complicated notation.

2.6 Density of phonon states

To further explore the phononic properties of materials, it is often useful to study the density of states function $g(\omega)$ and its strict relation with the dispersion curve branches $\omega_\lambda(\vec{q})$.
In particular, the quantity $g(\omega)d\omega$ actually corresponds to the number of vibrational states with frequency between ω and $\omega + d\omega$. This implies the necessity to require a normalization condition that, in the most general case, takes the form of Equation (2.4.0.2) as the number of normal modes of a N-ions lattice is $3N$.
In Section 2.5.3 and 2.5.4 it is shown that the phononic dispersion curve of a 3D Bravais lattice can exhibit more branches $\omega_\lambda(\vec{q})$ indexed by an integer λ unless local degenerations over the chosen high symmetry lines in the first Brillouin zone. For each of those branches a partial density of states function $g_\lambda(\omega)$ can be defined such that

$$\sum_\lambda g_\lambda(\omega) = \sum_{\lambda,\vec{q}} \delta(\omega - \omega_\lambda(\vec{q})) = g(\omega) \tag{2.6.0.1}$$

where the points $\vec{q}$ in the first Brillouin zone form a discrete set due to the imposition of the Born-von Karman boundary conditions, as explained in Section 2.5.
In the 3D case, the partial density of states associated to a generic dispersion branch is given by

$$g_\lambda(\omega) = \left(\frac{2\pi}{L}\right)^{-3} \int_S \frac{ds}{|\nabla_{\vec{q}}\, \omega_\lambda(\vec{q})|} \tag{2.6.0.2}$$

where $\left(\frac{2\pi}{L}\right)$ is the elementary unit of reciprocal space due to a 3D lattice, whose volume is approximately cubic of side L and equal to L^3, while S is a surface of same frequency ω in the first Brillouin zone.

2.6.1 Example of a 1D monoatomic linear chain

Now, consider a 1D monoatomic linear chain, whose phononic dispersion curve is obtained step-by-step in Section 2.5.1 and it is written explicitly in Equation (2.5.1.5). The group velocity can be thus calculated by the following derivative

$$\begin{aligned}\frac{d\omega}{dq} &= \sqrt{\frac{4k}{m}}\frac{a}{2}\cos\left(\frac{qa}{2}\right) = \frac{a}{2}\sqrt{\frac{4k}{m} - \frac{4k}{m}\sin^2\left(\frac{qa}{2}\right)} = \\ &= \frac{a}{2}\sqrt{\frac{4k}{m} - \omega^2(q)}\end{aligned} \tag{2.6.1.1}$$

and consequently one gets its inverse as

$$\frac{dq}{d\omega} = \left(\frac{d\omega}{dq}\right)^{-1} = \frac{2}{a\sqrt{\frac{4k}{m} - \omega^2}}. \tag{2.6.1.2}$$

Further, in case of an atomic chain of length L, the number of vibrational states $dN(q)$ with wave number between q and $q + dq$ is

$$dN(q) = 2\left(\frac{L}{2\pi}\right)dq \quad \Rightarrow \quad \frac{dN}{dq} = \frac{L}{\pi} \tag{2.6.1.3}$$

taking into account both negative and positive values for q.
Hence the density of states can be expressed as

$$g(\omega) = \frac{dN}{d\omega} = \frac{dN}{dq}\frac{dq}{d\omega} \tag{2.6.1.4}$$

which explicitly becomes

$$g(\omega) = \frac{2L}{\pi a\sqrt{\frac{4k}{m} - \omega^2}} \tag{2.6.1.5}$$

by substituting the results in Equations (2.6.1.2) and (2.6.1.3) into the product in (2.6.1.4). An exemplary plot of this function is shown in Figure 2.11.
For $\omega = 0$, it clearly admits a non-zero value equal to

$$g(\omega = 0) = \frac{2L}{\pi a\sqrt{\frac{4k}{m}}} = \frac{L}{\pi a}\sqrt{\frac{m}{k}}, \tag{2.6.1.6}$$

while for $\omega = \sqrt{\frac{4k}{m}}$ the denominator in Equation (2.6.1.5) vanishes and this implies a divergence to $+\infty$ for the density of states function.

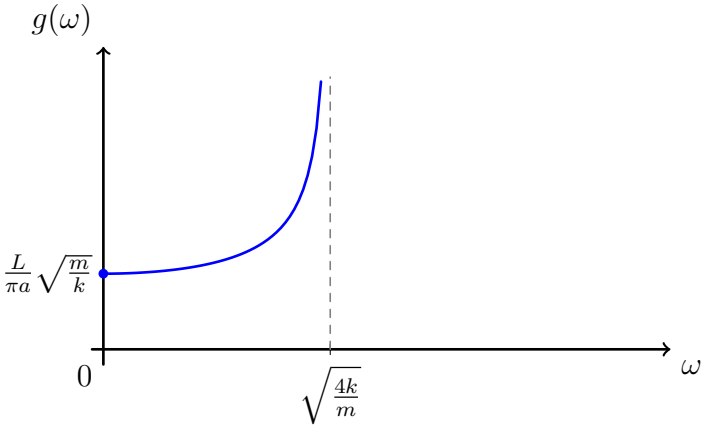

Figure 2.11: *The density of phonon states for a 1D monoatomic linear chain.*

2.6.2 Critical points and van Hove singularities

In general, for a 3D Bravais lattice the density of phonon states can exhibit very peculiar structures, that mainly derive from the existence of reciprocal space vectors $\vec{q}_{cp}$ such that $|\nabla_{\vec{q}}\, \omega_\lambda(\vec{q} = \vec{q}_{cp})| = 0$ involving a zero denominator in Equation (2.6.0.2). These special wave vectors $\vec{q}_{cp}$ are said critical points of the generic λ-th branch $\omega_\lambda(\vec{q})$ of the phononic dispersion relation and they correspond to the so called van Hove singularities for the density of states function.
For better understanding what such singularities consist in, it is useful to study the topology of the dispersion branch $\omega_\lambda(\vec{q})$ in proximity of a critical point $\vec{q}_{cp}$. Then, its Taylor series expansion at the lowest possible order of approximation for $|\vec{q} - \vec{q}_{cp}| \to 0$ is given by

$$\omega_\lambda(\vec{q}) = \omega_\lambda(\vec{q}_{cp}) + \sum_{i=1}^{3} \alpha_i (\vec{q} - \vec{q}_{cp})_i^2 \tag{2.6.2.1}$$

where α_1, α_2, α_3 are three real coefficients whose sign basically specifies the classification of the critical point $\vec{q}_{cp}$ under study.
If they are all positive or negative, respectively the dispersion curve $\omega_\lambda(\vec{q})$ will present a minimum or a maximum in $\vec{q}_{cp}$; but if at least one of them has a discordant sign with respect to the others, $\vec{q}_{cp}$ will be a saddle point.
This is indeed the reason why often such critical points are ranked according to the number of negative coefficients among α_1, α_2, α_3, as illustrated in Tables 2.2.
In addition, there is a theorem that provides the minimum number C_n^N of critical points of type M_n with $n \leq N$, if the associated dispersion curve is periodic and analytical in N variables, as follows

$$C_n^N = \frac{N!}{n!\ (N-n)!}. \tag{2.6.2.2}$$

Negative Coefficients	Symbol	Class
0	M_0	minimum
1	M_1	maximum

(a)

Negative Coefficients	Symbol	Class
0	M_0	minimum
1	M_1	saddle
2	M_2	maximum

(b)

Negative Coefficients	Symbol	Class
0	M_0	minimum
1	M_1	saddle
2	M_2	saddle
3	M_3	maximum

(c)

Table 2.2: *Schematic representation of the critical point classification for 1D* (a)*, 2D* (b) *and 3D crystal lattices* (c) *in terms of the number of negative coefficients in the Taylor series expansion of the dispersion relation.*

This means that in the 1D case ($N = 1$ and $n = 0, 1$) the branch will exhibit at least $C_0^1 = 1$ minimum and $C_1^1 = 1$ maximum; in the 2D case ($N = 2$ and $n = 0, 1, 2$), it will have instead $C_0^2 = 1$ minimum, $C_1^2 = 2$ saddle points and $C_2^2 = 1$ maximum; in the 3D case ($N = 3$ and $n = 0, 1, 2, 3$), it will finally present $C_0^3 = 1$ minimum, $C_1^3 = 3$ saddle points of type M_1, $C_2^3 = 3$ saddle points of type M_2 and $C_3^3 = 1$ maximum.
Furthermore, another theorem states that in the 3D case there are four different frequencies $\omega_0 < \omega_1 < \omega_2 < \omega_3$, in proximity of which critical points of type M_i tend to show with i as the index of the associated frequency. So, the overall trend of the density of states will seem to be characterized by only four van Hove singularities, instead of the eight required.
In order to study the nature of the reciprocal space surfaces that solve the Equation (2.6.2.1), the more useful cylindrical coordinates (q, θ, q_z) are introduced by the following transformations

$$\begin{cases} q^2 = q_1^2 + q_2^2 \\ \tan\theta = \frac{q_2}{q_1} \\ q_z = q_3 \end{cases} \quad \Rightarrow \quad \begin{cases} q = \sqrt{q_1^2 + q_2^2} \\ \theta = \tan^{-1}\left(\frac{q_2}{q_1}\right) \\ q_z = q_3 \end{cases} \tag{2.6.2.3}$$

from the canonical ones (q_1, q_2, q_3).
The Taylor series expansion can be thus rewritten as

$$\omega_\lambda(\vec{q}) - \omega_\lambda(\vec{q}_{cp}) = \alpha_1 q^2 + \alpha_3 q_z^2 \tag{2.6.2.4}$$

hypothesizing that $\alpha_1 = \alpha_2$.
In case of a critical point $\vec{q}_{cp}$ of type M_0, one can deduce that $\omega_\lambda(\vec{q}_{cp}) \simeq \omega_0$ and $\alpha_1, \alpha_3 > 0$; so, the equation describes an ellipsoidal surface for $\omega_\lambda(\vec{q}) > \omega_0$, but also it does not admit solution for $\omega_\lambda(\vec{q}) < \omega_0$.
Differently, if $\vec{q}_{cp}$ is a critical point of type M_1, then $\omega_\lambda(\vec{q}_{cp}) \simeq \omega_0$ and $\alpha_1 > 0, \alpha_3 < 0$ must be valid. These results lead to hyperboloids, that are of one sheet for $\omega_\lambda(\vec{q}) > \omega_1$ and of two sheets for $\omega_\lambda(\vec{q}) < \omega_1$.
Critical points $\vec{q}_{cp}$ of type M_2 instead show fully specular features with respect to the previous case. Indeed, having $\omega_\lambda(\vec{q}_{cp}) \simeq \omega_2$ and $\alpha_1 < 0, \alpha_3 > 0$, the hyperboloidal solutions are of one sheet for $\omega_\lambda(\vec{q}) < \omega_2$ and of two sheets for $\omega_\lambda(\vec{q}) > \omega_2$.
Finally, the case of a critical point $\vec{q}_{cp}$ of type M_3 is the opposite of the first, because basically $\alpha_1, \alpha_3 < 0$. This implies that, being $\omega_\lambda(\vec{q}_{cp}) \simeq \omega_3$, the equation describes an ellipsoidal surface for $\omega_\lambda(\vec{q}) < \omega_3$, but it does not admit solution for $\omega_\lambda(\vec{q}) > \omega_3$.
The just discussed topological results regarding the solution of Equation (2.6.2.4) are summarized in a more intuitive way in Table 2.3.

Type	Frequency Ranges	Surfaces
M_0	$\omega < \omega_0$	No solution
	$\omega > \omega_0$	Ellipsoid
M_1	$\omega < \omega_1$	Hyperboloid of two sheets
	$\omega > \omega_1$	Hyperboloid of one sheet
M_2	$\omega < \omega_2$	Hyperboloid of one sheet
	$\omega > \omega_2$	Hyperboloid of two sheets
M_3	$\omega < \omega_3$	Ellipsoid
	$\omega > \omega_3$	No solution

Table 2.3: *Overview of the reciprocal space surfaces that solve the Equation* (2.6.2.4) *for each possible type of critical point, indicating* $\omega_\lambda(\vec{q})$ *with* ω *for simplicity.*

Such surfaces can be selected so as to be symmetric to the q_z axis, and it can be demonstrated that the partial density of states $g_\lambda(\omega)$ is actually proportional to their projection on the plane normal to that axis near the critical point $\vec{q}_{cp}$. This considerably simplifies the calculation of the density of states function, reducing the Equation (2.6.0.2) to an integral on the variable q_z, whose domain depends firstly on the energy surface, but indirectly also on the classification of the critical point.

Indeed, in case of an ellipsoidal surface, the only possible types of critical point are M_0 or M_3, and the coordinate q_z is revealed to be in the real interval

$$-\sqrt{\frac{|\omega_\lambda(\vec{q})-\omega_i|}{\alpha_3}} \leq q_z \leq \sqrt{\frac{|\omega_\lambda(\vec{q})-\omega_i|}{\alpha_3}} \quad \text{with} \quad i=0,3 \tag{2.6.2.5}$$

So, the associated density of states takes the form

$$g_\lambda(\omega) \propto \begin{cases} \sqrt{\omega-\omega_0} & \text{for} \quad i=0 \quad \text{and} \quad \omega>\omega_0 \\ \sqrt{\omega_3-\omega} & \text{for} \quad i=3 \quad \text{and} \quad \omega<\omega_3 \end{cases} \tag{2.6.2.6}$$

which for clarity is shown in the graphs of Figure 2.12.

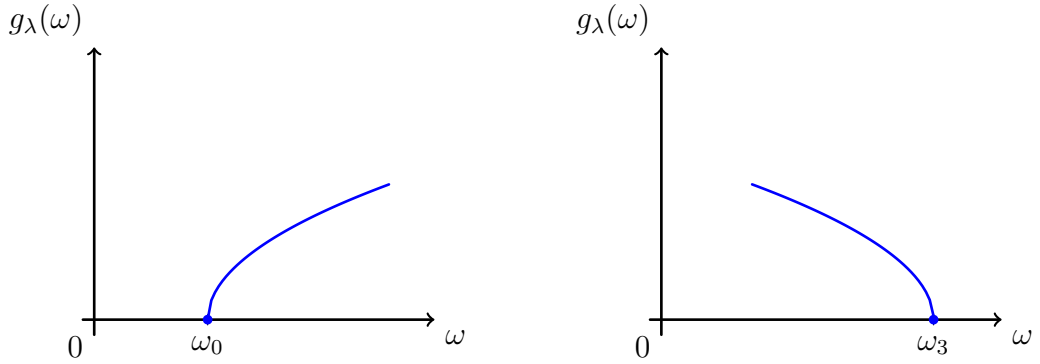

Figure 2.12: *The density of phonon states behaviour in proxity of a M_0 (left) and M_3 (right) van Hove singularity.*

Otherwise, for an hyperboloidal surface which can be traced back only to critical points of type M_1 or M_2, the q_z domain is

$$\begin{cases} q_z \in \mathbb{R} - \left(-\sqrt{\frac{|\omega_\lambda(\vec{q})-\omega_i|}{\alpha_3}}; +\sqrt{\frac{|\omega_\lambda(\vec{q})-\omega_i|}{\alpha_3}}\right) & \text{if 2 sheets and } i=1,2 \\ q_z \in \mathbb{R} & \text{if 1 sheet.} \end{cases} \tag{2.6.2.7}$$

Therefore, one can obtain the density of states to exhibit an infinite or finite slope respectively for the first or second case in Equation (2.6.2.7). Indeed, M_1 and M_2 van Hove singularities usually appear to be similar to the trends in Figure 2.13.

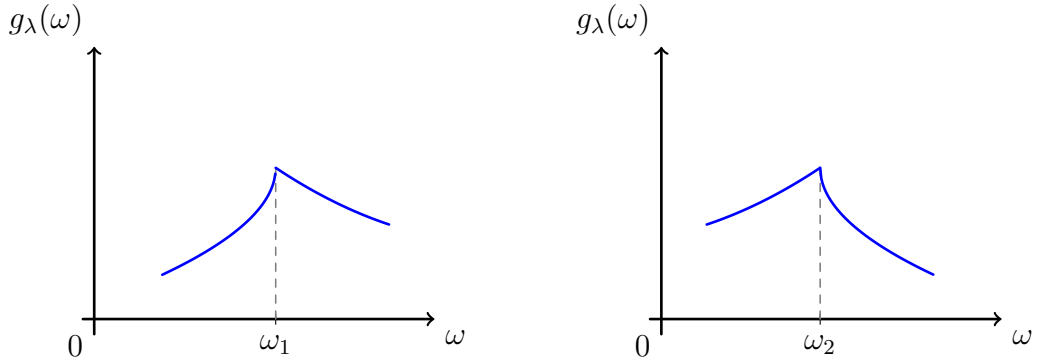

Figure 2.13: *The density of phonon states behaviour in proximity of a M_1 (left) and M_2 (right) van Hove singularity.*

Now, the whole shape of the function $g_\lambda(\omega)$ can be assembled and in the simplest case where the M_1 and M_2 singularities are degenerate it looks like the graph in Figure 2.14.

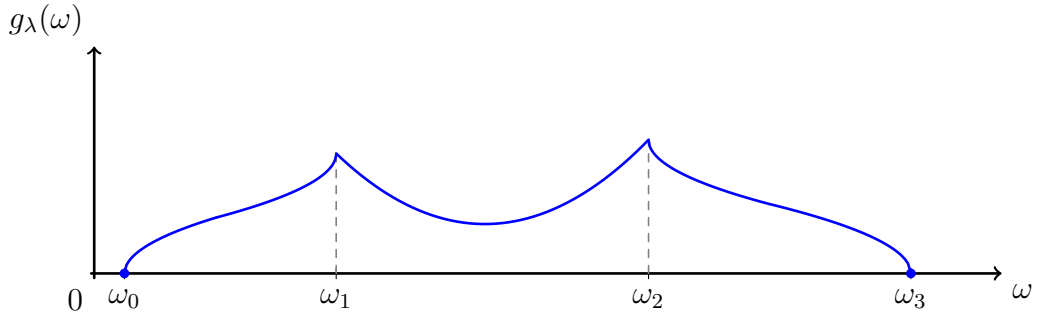

Figure 2.14: *The partial density of phonon states associated with an optic dispersion branch.*

However, these results cannot be valid for the acoustic branches $\omega_\lambda(\vec{q})$, because of their high wavelength limit

$$\lim_{q\to 0} \omega_\lambda(\vec{q}) = 0 \tag{2.6.2.8}$$

which means that the dispersion curve is not analytical for $|\vec{q}| = 0$.
Hence the only difference of the partial densities of states of acoustic branches from those of optic branches is the low frequency behaviour, which is found to be $g_\lambda(\omega) \propto \omega^2$ for $\omega \to 0$ just as the Debye model result in Equation (2.4.0.8). They thus take the form in Figure 2.15.

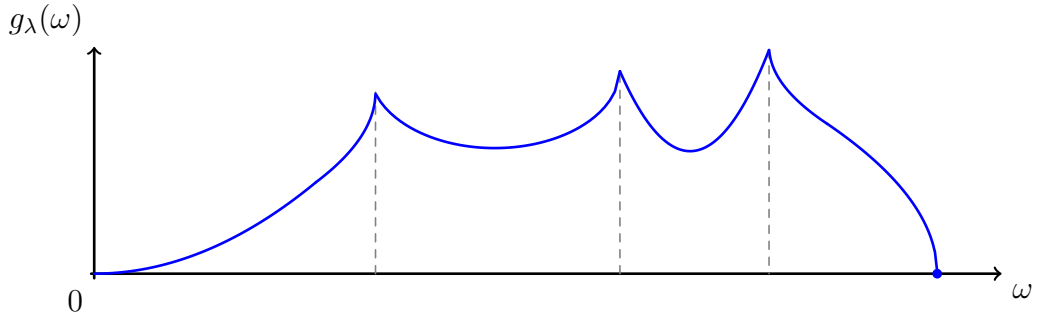

Figure 2.15: *The partial density of phonon states associated with an acoustic dispersion branch.*

Chapter 3

Computational analyses of fcc Bravais lattice of diamond Carbon

3.1 *Ab initio* calculations

The many-body Schrödinger problem is the starting point for the development of the quantum theory of materials modeling and its solving techniques are then executed by most of the computer programs working on the implementation of *ab initio* calculations of materials properties, just like VASP. It consists in finding the energy eigenvalues of a system of N electrons with coordinates $\vec{r}_1, \vec{r}_2, ..., \vec{r}_N$ and M nuclei with coordinates $\vec{R}_1, \vec{R}_2, ..., \vec{R}_M$, subjected to either attractive or repulsive Coulombic interaction potentials. The so called many-body Hamiltonian thus takes the form

$$\hat{H} = \hat{K}_e + \hat{K}_n + \hat{U}_{ee} + \hat{U}_{en} + \hat{U}_{nn}. \tag{3.1.0.1}$$

The first two terms ($\hat{K}_e$, $\hat{K}_n$) are the kinetic energies

$$\hat{K}_e = -\frac{\hbar^2}{2m_e}\sum_{i=1}^{N}\nabla_i^2 \qquad \hat{K}_n = -\sum_{n=1}^{M}\frac{\hbar^2}{2M_n}\nabla_n^2 \tag{3.1.0.2}$$

with m_e and M_n respectively indicate the mass of electron and that of the n-th nucleus, while the others are the Coulombic potential energies of electrons-electrons and nuclei-nuclei repulsion ($\hat{U}_{ee}$, $\hat{U}_{nn}$)

$$\hat{U}_{ee} = \frac{1}{4\pi\varepsilon_0}\frac{1}{2}\sum_{\substack{i,j=1\\ i\neq j}}^{N}\frac{e^2}{|\vec{r}_i - \vec{r}_j|} \qquad \hat{U}_{nn} = \frac{1}{4\pi\varepsilon_0}\frac{1}{2}\sum_{\substack{n,m=1\\ n\neq m}}^{M}\frac{Z_n Z_m e^2}{|\vec{R}_n - \vec{R}_m|}, \tag{3.1.0.3}$$

and electrons-nuclei attraction ($\hat{U}_{en}$)

$$\hat{U}_{en} = -\frac{1}{4\pi\varepsilon_0}\sum_{n=1}^{M}\sum_{i=1}^{N}\frac{Z_n e^2}{|\vec{r}_i - \vec{R}_n|} \tag{3.1.0.4}$$

with Z_n as the atomic number of the n-th nucleus.
The wave function ψ of the system depends on the coordinates of each electron and nucleus

$$\psi = \psi(\vec{r}_1, \vec{r}_2, ..., \vec{r}_N; \vec{R}_1, \vec{R}_2, ..., \vec{R}_M) \tag{3.1.0.5}$$

and its square modulus $|\psi|^2$ thus represents the probability of finding all the subsystems in an arbitrary spatial configuration.
Hence the many-body Schrödinger equation can be written as

$$\hat{H}\psi = E_{tot}\psi, \tag{3.1.0.6}$$

but it cannot be solved analytically for the eigenvalue E_{tot} due to its remarkable complexity.
However, in case of solid crystal lattices, the nuclei do not move much from their equilibrium positions with respect to the electronic motions and this is actually result of the scale of their masses $m_e \ll M_n \ \forall n \in \{1, 2, ..., M\}$. In this way, the so called clamped nuclei approximation is taken into account and allows not only to neglect the kinetic energy $\hat{K}_n$, but also to reduce the potential $\hat{U}_{nn}$ to a constant shift, having the coordinates $\vec{R}_1, \vec{R}_2, ..., \vec{R}_M$ fixed. For the same reason, the Born-Oppenheimer approximation can be applied to the total wave function, that thus reduces to the tensor product of its electronic and nuclear components as follows

$$\psi = \psi_e(\vec{r}_1, \vec{r}_2, ..., \vec{r}_N) \otimes \psi_n(\vec{R}_1, \vec{R}_2, ..., \vec{R}_M). \tag{3.1.0.7}$$

Therefore, the Equation (3.1.0.6) for the electronic component ψ_e simplifies to

$$\hat{H}_e\psi_e = [\hat{K}_e + \hat{U}_{ee} + \hat{U}_{en}]\psi_e = E\psi_e \tag{3.1.0.8}$$

where $\hat{H}_e$ is called the many-electron Hamiltonian and presents E as the electronic energy eigenvalue given by

$$E = E_{tot} - \frac{1}{8\pi\varepsilon_0} \sum_{\substack{n,m=1 \\ n \neq m}}^{M} \frac{Z_n Z_m e^2}{|\vec{R}_n - \vec{R}_m|}. \tag{3.1.0.9}$$

Now, the single-electron Hamiltonian $\hat{H}_0(\vec{r})$ can be defined as

$$\hat{H}_0(\vec{r}) = -\frac{\hbar^2}{2m_e}\nabla^2 - \frac{1}{4\pi\varepsilon_0} \sum_{n=1}^{M} \frac{Z_n e^2}{|\vec{r} - \vec{R}_n|} = -\frac{\hbar^2}{2m_e}\nabla^2 + \hat{V}_n(\vec{r}) \tag{3.1.0.10}$$

so that the previous $\hat{H}_e$ explicitly reads as

$$\hat{H}_e = \sum_{i=1}^{N} \hat{H}_0(\vec{r}_i) + \hat{U}_{ee}. \tag{3.1.0.11}$$

Actually, the appearance of the electrons-electrons Coulombic repulsive potential $\hat{U}_{ee}$ in Equation (3.1.0.11) makes the problem still unsolvable; so, two different approaches are possible: the independent electrons approximation (less accurate) or the mean-field approximation (more realistic).
The first consists in the rather drastic hypothesis of eliminating the electrons-electrons interaction term such that the many-electron Schrödinger equation simplifies to

$$\sum_{i=1}^{N} \hat{H}_0(\vec{r}_i)\psi_e = E\psi_e. \tag{3.1.0.12}$$

Thus, it is possible to write the wave function ψ_e as a product of single-electron wave functions $\phi_i(\vec{r}_i)$ with $i = 1, 2, ..., N$ that satisfy the following single-electron Schrödinger equations

$$\hat{H}_0(\vec{r}_i)\phi_i(\vec{r}_i) = \varepsilon_i\phi_i(\vec{r}_i) \tag{3.1.0.13}$$

with ordered energy eigenvalues $\varepsilon_1 < \varepsilon_2 < ... < \varepsilon_N$.
Substituting the result in Equation (3.1.0.13) into (3.1.0.12), one can easily find the solution to the many-electron Schrödinger equation, as the energy eigenvalue E is given by

$$E = \varepsilon_1 + \varepsilon_2 + ... + \varepsilon_N \tag{3.1.0.14}$$

which means that the N electrons of the system arrange in the lowest-energy configuration, obeying to the condition of permutational antisymmetry on the wave function ψ required by the Pauli exclusion principle for fermions.
However, the initial assumption of neglecting the Coulombic potential $\hat{U}_{ee}$ in the independent electrons approximation is completely disconfirmed by its order of magnitude with respect to the other terms. So, the second approach aims to reintroduce that interaction in terms of the average potential $\hat{V}_H(\vec{r})$, called Hartree potential, experienced by each electron

$$\hat{V}_H(\vec{r}) = \frac{1}{4\pi\varepsilon_0}\int d\vec{r}\,' \frac{\rho(\vec{r}\,')}{|\vec{r} - \vec{r}\,'|} \tag{3.1.0.15}$$

with $\rho(\vec{r}) = \sum_{i=1}^{N} |\phi_i(\vec{r})|^2$ as the electron density given by the sum of the probabilities of finding each electron in the position $\vec{r}$.
The procedure for the solution is basically founded on the following variational principle. First, considering the ground state ψ_0 as a Slater determinant of the single-electron wave functions, its energy functional E_0 is calculated by the integral

$$E_0 = \int d\vec{r}_1 ... d\vec{r}_N \ \psi_0^* \hat{H}_e \psi_0. \tag{3.1.0.16}$$

Second, if one impose the minimization of the energy functional with respect to $\phi_i(\vec{r}_i)$

$$\frac{\delta E_0}{\delta \phi_i^*} = 0 \qquad \forall i \in \{1, 2, ..., N\} \tag{3.1.0.17}$$

and the orthonormality condition of such functions

$$\int d\vec{r}\ \phi_i^*(\vec{r})\phi_j(\vec{r}) = \delta_{i,j} \qquad \forall i,j \in \{1,2,...,N\}, \tag{3.1.0.18}$$

then it can be shown that the Hartree-Fock equations are obtained as

$$\begin{cases} \left[\hat{H}_0(\vec{r}) + \hat{V}_H(\vec{r})\right]\phi_i(\vec{r}) + \int d\vec{r}\,'\ \hat{V}_X(\vec{r},\vec{r}\,')\phi_i(\vec{r}\,') = \varepsilon_i\phi_i(\vec{r}) \\ \nabla^2\hat{V}_H(\vec{r}) = -\varepsilon_0^{-1}\rho(\vec{r}). \end{cases} \tag{3.1.0.19}$$

The last one is known as Poisson equation and the function $\hat{V}_X(\vec{r},\vec{r}\,')$ is the so called Fock exchange potential, whose explicit expression is

$$\hat{V}_X(\vec{r},\vec{r}\,') = -\frac{1}{4\pi\varepsilon_0}\sum_j \frac{\phi_j^*(\vec{r}\,')\phi_j(\vec{r})}{|\vec{r}-\vec{r}\,'|} \tag{3.1.0.20}$$

with the index j that takes the integral values associated with single-electron wave functions ϕ_j having the same spin as ϕ_i in the first of the Equations (3.1.0.19).
The solutions $\phi_i(\vec{r})$ for the Hartree-Fock equations must be such that the resulting potential $\hat{V}_H(\vec{r})$ is self-consistent with its initial guess and also admits same solutions $\phi_i(\vec{r})$ if it is reinserted in Equations (3.1.0.19). Consequently, the electronic component ψ_e of the many-body wave function can be expressed as a Slater determinant of such $\phi_i(\vec{r})$ in order to satisfy the Pauli exclusion principle. At the same time, the minimum for the electronic energy functional E_0 is further estimated and depends on the lattice structure given by the previously fixed nuclear coordinates $\vec{R}_n$.
Thus, the so calculated electronic energy $E_0(\{\vec{R}_n\})$ can be reinterpreted as a sort of $3M$-dimensional potential energy in the many-body Schrödinger equation for the nuclear component ψ_n

$$\left[\hat{K}_n + \hat{U}_{nn} + E_0(\{\vec{R}_n\})\right]\psi_n = E_{tot}\psi_n. \tag{3.1.0.21}$$

reintroducing the nuclear kinetic energy $\hat{K}_n$.
Finally, the equilibrium lattice structure can be approximated by numerical algorithms, such as steepest descent or conjugate gradients methods, for the minimization of the potential energy experienced by the M nuclei.
Another popular tool among materials modeling programs is the density functional theory, often shortened to DFT, which aims at computing the total energy E_0 of many electrons in their ground state. For the Hohenberg-Kohn theorem such quantity can be written as the following functional of the electron density $\rho(\vec{r})$

$$\begin{aligned} E_0 = F[\rho] = \langle\psi_e[\rho]|\hat{H}_e|\psi_e[\rho]\rangle = &\int d\vec{r}\rho(\vec{r})\hat{V}_n(\vec{r}) + \frac{1}{2}\int d\vec{r}\rho(\vec{r})\hat{V}_H(\vec{r}) \\ &- \frac{\hbar^2}{2m_e}\sum_i \int d\vec{r}\phi_i^*(\vec{r})\nabla^2\phi_i(\vec{r}) + E_{xc}[\rho] \end{aligned} \tag{3.1.0.22}$$

where the extra term $E_{xc}[\rho]$ is called exchange and correlation energy and gives an unknown contribution to the total electronic energy.
Now, the Hohenberg-Kohn variational principle can be applied by imposing the minimization condition of the functional $F[\rho]$ at the ground-state electron density ρ_0

$$\left.\frac{\delta F[\rho]}{\delta \rho}\right|_{\rho_0} = 0 \tag{3.1.0.23}$$

which leads to the Kohn-Sham equations that read as

$$\begin{cases} \left[-\frac{\hbar^2}{2m_e}\nabla^2 + \hat{V}_n(\vec{r}) + \hat{V}_H(\vec{r}) + \hat{V}_{xc}(\vec{r})\right]\phi_i(\vec{r}) = \varepsilon_i\phi_i(\vec{r}) \\ \nabla^2\hat{V}_H(\vec{r}) = -\varepsilon_0^{-1}\rho(\vec{r}) \\ \hat{V}_{xc}(\vec{r}) = \frac{\delta E_{xc}[\rho]}{\delta\rho}(\vec{r}). \end{cases} \tag{3.1.0.24}$$

However, the energy eigenvalues ε_i and the eigenfunctions $\phi_i(\vec{r})$ which constitute the solutions of the problem can be obtained explicitly only if the total potential $\hat{V}_{tot}(\vec{r}) = \hat{V}_n(\vec{r}) + \hat{V}_H(\vec{r}) + \hat{V}_{xc}(\vec{r})$ is known as function of the electron density $\rho(\vec{r})$. It implies that each solution $\phi_i(\vec{r})$ depends on all other $\phi_j(\vec{r})$ with $j \neq i$.
Therefore, the whole procedure must grant their self-consistency, which means that if the first solutions $\phi_i(\vec{r})$ are inserted into the electron density formula in order to calculate the new total potential expression and the Kohn-Sham equations are dealt with again, then the second solutions $\phi'_i(\vec{r})$ turn out to be the same as the previous ones.
So, the total electronic energy in the ground state can be computed by constructing increasingly better estimates of the electron density $\rho(\vec{r})$ until the self-consistency is finally achieved within a desired tolerance.

3.2 Ionic relaxation

The first procedure consists in the ionic relaxation of the fcc lattice of diamond Carbon, which is obtained by VASP via the minimization of the total energy of the system, as anticipated in Section 3.1.
The execution of such a task requires the preparation of four Input files, called POSCAR, KPOINTS, INCAR and POTCAR.
The POSCAR file provides the necessary information about the spatial configuration of the lattice as follows

```
system C
3.730
0.5 0.5 0.0
0.0 0.5 0.5
0.5 0.0 0.5
C
2
cart
0.00 0.00 0.00
0.25 0.25 0.25
```

and contains in order an initial comment line that can be used for introducing the name of the system under study, a guess of the lattice constant a_g (in Å) that is later used as a scale factor for the lattice vectors, the 3D lattice vectors $\vec{a}_1, \vec{a}_2, \vec{a}_3$ defining the unit cell structure, the atom symbol, the number of atoms per unit cell, an indicator of the choice of coordinate system and finally the coordinates of the atoms in the unit cell. In particular, the only allowed coordinate systems are Cartesian and Direct, which respectively allow to specify an arbitrary 3D vector $\vec{R}$ via three real coefficients (x, y, z) or (R_1, R_2, R_3) as

$$\vec{R} = \begin{cases} a_g(x\vec{u}_x + y\vec{u}_y + z\vec{u}_z) & \text{(Cartesian)} \\ R_1\vec{a}_1 + R_2\vec{a}_2 + R_3\vec{a}_3 & \text{(Direct)} \end{cases} \tag{3.2.0.1}$$

where $\vec{u}_x, \vec{u}_y, \vec{u}_z$ are the versors forming the 3D Cartesian orthonormal basis.
The KPOINTS file instead includes details of the reciprocal space sampling during the procedure and in this case it has the basic form

```
Regular k-points mesh
0
Gamma
7  7  7
0  0  0
```

As POSCAR, the first line is regarded as a comment, while by the zero in the second is meant that the sample is automatically generated by a regular mesh, whose center (`Gamma`=(0,0,0) in reciprocal space) is specified immediately after. At last, the other two triples of numbers respectively set the sample number (N_1, N_2, N_3) along each reciprocal lattice vector $(\vec{b}_1, \vec{b}_2, \vec{b}_3)$ and the optional shift (s_1, s_2, s_3) of the mesh generation.
In particular, as the 3D reciprocal lattice vectors for a generic fcc lattice are

$$\vec{b}_1 = \frac{2\pi}{a_g}(-1, 1, 1) \quad \vec{b}_2 = \frac{2\pi}{a_g}(1, -1, 1) \quad \vec{b}_3 = \frac{2\pi}{a_g}(1, 1, -1), \tag{3.2.0.2}$$

the sample generated by the mesh in the first Brillouin zone is given by the k-points $\vec{q}^{\,(j)}$ with $j = 1, 2, ..., N_1 N_2 N_3$

$$\vec{q}^{\,(j)} = \sum_{i=1}^{3} \frac{n_i^{(j)} + s_i}{N_i} \, \vec{b}_i \qquad \text{for } n_i^{(j)} \in 0, 1, 2, ..., N_i. \tag{3.2.0.3}$$

Next, the INCAR file includes the instructions on what task to be performed and how to do it, in a "tag = value" syntax. In this case, the main tags are chosen to be

```
ALGO = Fast
EDIFF = 0.0004
ENCUT = 520
PREC = Accurate
IBRION = 2
ISIF = 3
```

The `ALGO = Fast` specifies an electronic minimization algorithm that follows each ionic update. Then, the `EDIFF` and `ENCUT` tags indicate two energy values in units of eV that respectively act as the lower energy limit for stopping the algorithm and the cutoff kinetic energy for the ionic plane waves basis for each k-point read from the KPOINTS file. The `PREC = Accurate` instead allows to avoid any aliasing or wrap around errors (necessary for phonon calculations), while the `IBRION = 2` selects the task to be performed, that in this case consists in a ionic relaxation via the conjugate gradient algorithm summarized in the following steps:

1. ionic trial displacement along a search direction;
2. forces calculation with respect to the initial lattice configuration (read from the POSCAR file);
3. approximation of the minimum total energy by a cubic interpolation;
4. corrector ionic displacement towards the approximate minimum;
5. forces and energy values update;
6. other trial and corrector steps are performed until the lattice total energy is enough close to the minimum.

Finally, the `ISIF` tag determines how many and which degrees-of-freedom (ionic positions, cell colume, cell shape) are allowed to change. So, `ISIF = 3` means that all three are considered.
The last Input file (POTCAR) is a read-only file made available by VASP and contains

specific information about the atoms in the lattice, such as the pseudopotential, the mass, the number of valence electrons and the default cutoff energy (`ENMAX`) which is later compared to the `ENCUT` tag initialized in the INCAR file.
This procedure of ionic relaxation has been performed not only on a single unit cell, but also on $2 \times 2 \times 2$ and $3 \times 3 \times 3$ supercell structures, which just needed the production of more complex POSCAR files via the terminal commands of Phonopy

```
phonopy -d --dim="2 2 2" --cell=POSCAR-unitcell
phonopy -d --dim="3 3 3" --cell=POSCAR-unitcell
```

and the reduction of the number of k-point samples from 7 respectively to 5 and 3 per reciprocal lattice vector in the KPOINTS files.
The resulting Output files are several, but only the CONTCAR file is the one of interest, since it contains the optimal lattice geometry at the approximate minimum energy in form of a POSCAR file, which will be later used as Input file for the study of the phononic dispersion curves. The so obtained structures are shown in Figure 3.1 thanks to the VESTA (Visualization for Electronic and STructural Analysis [15]-[16]-[17]-[18]) software.

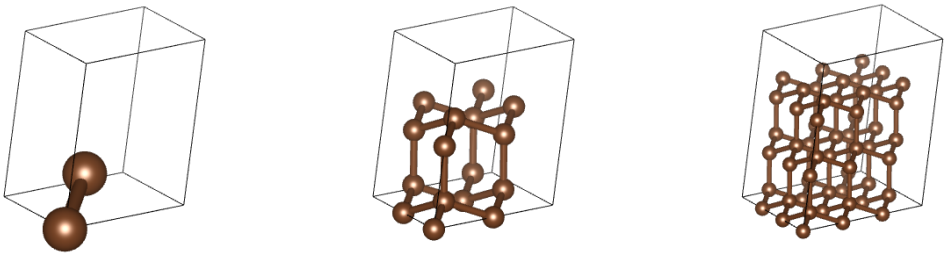

(a) (b) (c)

Figure 3.1: *3D visualization of the approximate lowest-energy configuration of a unit cell* (a), *a* $2 \times 2 \times 2$ *supercell* (b) *and a* $3 \times 3 \times 3$ *supercell* (c) *of the fcc lattice of diamond Carbon with interatomic bonds represented by fictitious sticks aiming at better understanding its three-dimensionality.*

Starting from the initial guess for the lattice step of 3.730 Å, these *ab initio* calculations for unit cell, $2 \times 2 \times 2$ and $3 \times 3 \times 3$ supercell structures for the fcc lattice of diamond Carbon respectively lead to three final estimates 3.561 Å, 3.557 Å and 3.556 Å, which are enough consistent with the experimental value of 3.57 Å found in [2].

3.3 Phononic dispersion

The *ab initio* calculations of the phononic dispersion curves require a two-steps procedure, which is performed initially by VASP and then by Phonopy.
In particular, the first step aims to compute the second-order force constants using a finite differences approach and thus to construct the dynamical matrix $\Delta^{(j,k)}(\vec{q})$, whose definition is written in Equation (2.5.4.3) for a generic 3D lattice. This is done by essentially reusing the same four Input files described in Section 3.2, except for the following modifications: the INCAR file must have the instruction `IBRION = 6` that sets the task to determine the second-order force constants and the dynamical matrix using six finite ionic displacements (default size of 0.015 Å) only along symmetry inequivalent directions and it also must have the ISIF tag canceled because the choice of degrees-of-freedom actually passes to the previous command. Then, all the results of the execution, as well as the initial data, are listed into an XML format file called `vasprun.xml`, which needs to be read via the Phonopy command

```
phonopy --fc vasprun.xml
```

in order to extract only data concerning force constants and write them into a text file named FORCE_CONSTANTS in a more easy-to-use format.
Now, as the second step of the procedure, the phonon frequencies have to be calculated and this can be performed by Phonopy through the preparation of a configuration file `band.conf` with the following "tag = value" statements

```
DIM = 2 2 2
ATOM_NAME = C

FULL_FORCE_CONSTANTS = .TRUE.
FORCE_CONSTANTS = READ
EIGENVECTORS = .TRUE.

BAND = 0 0 0  0.375 0.375 0.75, 0.625 0.25 0.625
       0.5 0 0.5  0 0 0 0.5 0.5 0.5
BAND_POINTS = 101
BAND_LABELS = $\Gamma$ K U X $\Gamma$ L
```

where essentially the first two lines give some basic information about the lattice, the `EIGENVECTORS = .TRUE.` specifies to prepare an Output file for the polarization eigenvectors of Equation (2.5.3.11) necessary for the subsequent modulation operation of atomic displacements near Γ, then the third and the fourth lines set the reading of the previously created FORCE_CONSTANTS file and finally the others specify the number of

k-points sampling and the high symmetry lines chosen for the evaluation of the phonon frequencies.
Once the `band.conf` file is ready, the Phonopy commands

```
phonopy --dim="2 2 2" --cell=POSCAR-unitcell band.conf
phonopy --dim="3 3 3" --cell=POSCAR-unitcell band.conf
```

can be runned depending on the supercell dimension and thus store the results in a YAML format file called `band.yaml`, which can be converted to a CSV file by a rather simple Python script. Hence the phonon band-structure for $2 \times 2 \times 2$ and $3 \times 3 \times 3$ supercell structures has been plotted and overlapped with the experimental data in [11] by the use of Matplotlib [19], NumPy [20] and SciPy [21] Python libraries in Figure 3.2.
Note that more unit cells the considered supercell structure includes, more the phononic dispersion relation can be evaluated precisely for generic k-points $\vec{q}$ different than zero. The reason behind this is attributed to the increasing possibilities of complex collective motion within the supercell. So, the study of the case of a single unit cell turns out to be practically useless, or better physically insignificant.
Indeed, the so obtained dispersion curves show an increasing compatibility to the experimental data by switching from $2 \times 2 \times 2$ to $3 \times 3 \times 3$ supercells.
Moreover, according to the actual fcc lattice of diamond Carbon, whose basis is formed by two Carbon atoms (so $p = 2$ from Section 2.5.4), they present 3 acoustic and $3(p-1) = 3$ optic branches with visible phenomena of degeneracy along some of the high symmetry lines, such as X-Γ and Γ-L where the capital letters stand for the following k-point in the first Brillouin zone

$$\begin{gathered} \Gamma = \frac{2\pi}{a}(0,0,0) \quad K = \frac{2\pi}{a}\left(\frac{3}{4},\frac{3}{4},0\right) \quad U = \frac{2\pi}{a}\left(1,\frac{1}{4},\frac{1}{4}\right) \\ X = \frac{2\pi}{a}(1,0,0) \quad L = \frac{2\pi}{a}\left(\frac{1}{2},\frac{1}{2},\frac{1}{2}\right) \end{gathered} \tag{3.3.0.1}$$

in Cartesian coordinates with a as the approximate lattice step.
Furthermore, those dispersion branches can be either classified as longitudinal or transverse depending on whether the atomic displacement vectors are parallel or perpendicular to the propagation direction of the collective wave. Thus in case of full non-degeneracy in proximity of the central k-point Γ, they can be labeled by LA, TA1, TA2, LO, TO1 and TO2, where L and T stand for longitudinal and transverse, A and O instead symbolize acoustic and optic and finally 1 and 2 distinguish the two possible transverse branches. The atomic motions associated with each of these dispersion curves has been represented via red vectors generated by VESTA in Figure 3.3 with an appropriate amplification to make their directions appreciable.

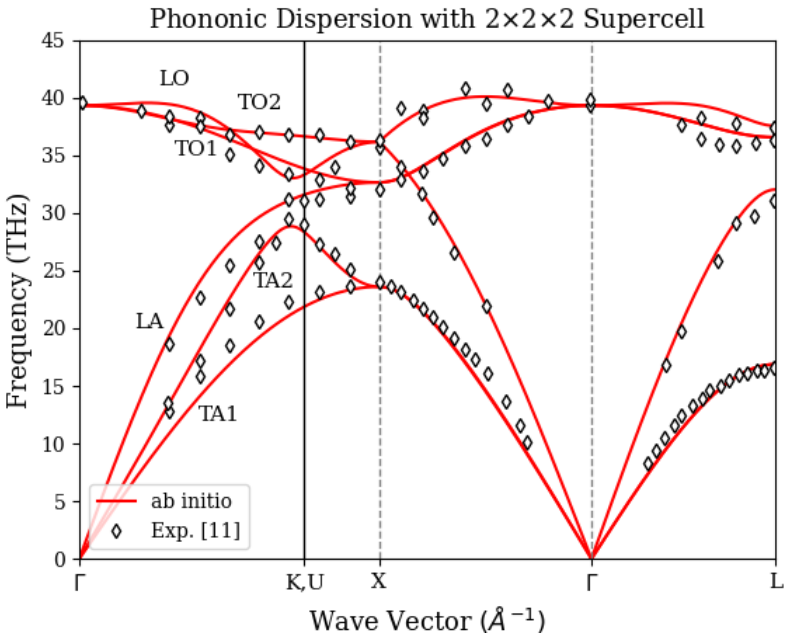
Phononic Dispersion with 2×2×2 Supercell
Frequency (THz)
Wave Vector (Å⁻¹)
LO
TO2
TO1
LA
TA2
TA1
ab initio
Exp. [11]
Γ
K,U
X
Γ
L

(a)

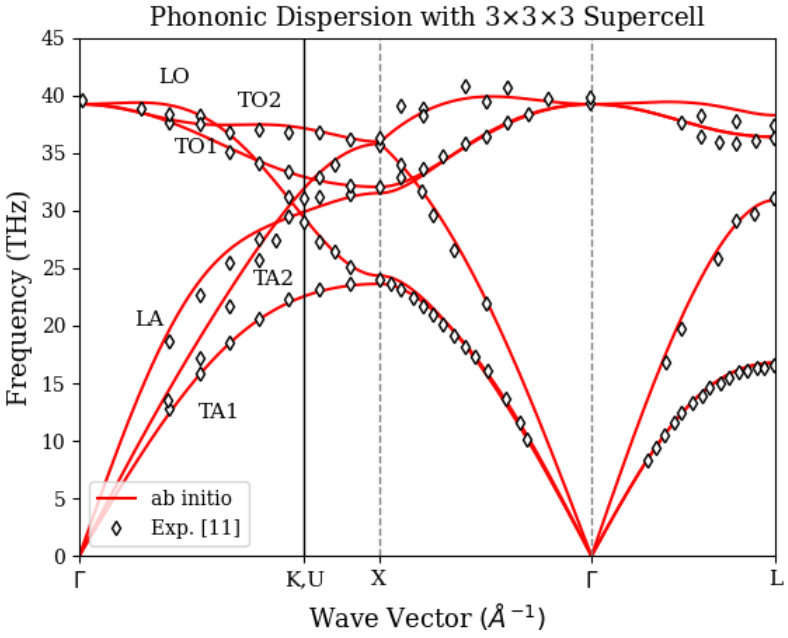
Phononic Dispersion with 3×3×3 Supercell
Frequency (THz)
Wave Vector (Å⁻¹)
LO
TO2
TO1
LA
TA2
TA1
ab initio
Exp. [11]
Γ
K,U
X
Γ
L

(b)

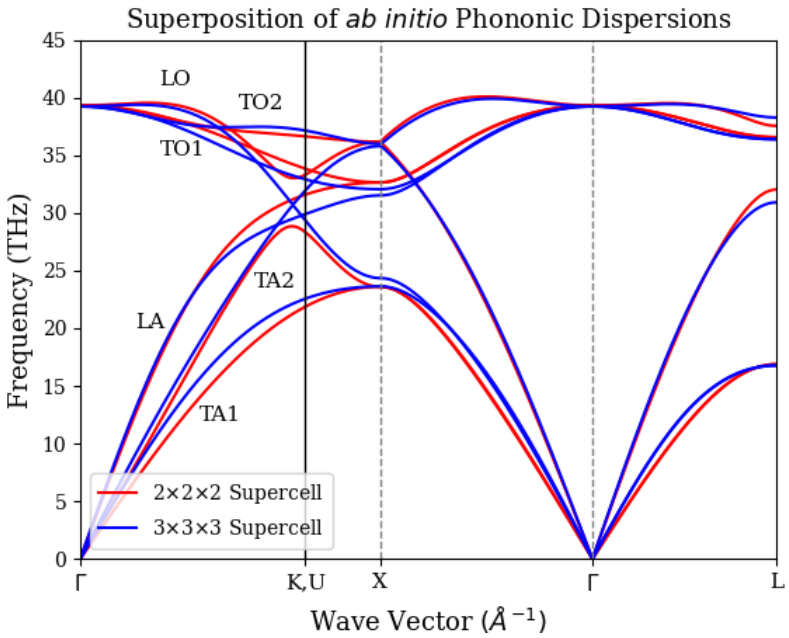

(c)

Figure 3.2: *Ab initio phononic dispersion curves for* $2 \times 2 \times 2$ (a) *and* $3 \times 3 \times 3$ *supercell structures* (b) *of fcc diamond Carbon overlapped with the experimental data in* [11] *along the high symmetry path* Γ-K,U-X-Γ-L *within the first Brillouin zone. The difference between these two ab initio results are evidenced in the third graph* (c).

For example, in order to realize the first 3D plot in Figure 3.3, it has been necessary to run the following Phonopy command on the terminal

```
phonopy --dim="3 3 3" --readfc --cell=POSCAR-unitcell
        --modulation="2 2 2, 0 0 0 1 10 0"
```

which creates a POSCAR-like file named MPOSCAR of a displaced $2 \times 2 \times 2$ supercell structure along the first dispersion branch near the k-point Γ with an amplification factor $A = 10$ and a phase shift $\varphi = 0$ indicated in the `modulation` option, but it also requires to specify the dimension of the starting supercell via `--dim="3 3 3"`, to set the reading of the force constants via `--readfc` and to name the POSCAR file of a single unit cell via `--cell=POSCAR-unitcell`. Then, varying only the seventh number in the `modulation` option from 1 to 6, the MPOSCAR files for the other plots can be obtained too.
In this way, the displacement of the j-th atom in the l-th unit cell is calculated from the

polarization vectors $\vec{\varepsilon}_s^{\,(j,0)}(\vec{q})$ as

$$\frac{A}{\sqrt{N_{sc}M_j}}\Re[e^{i\varphi}\vec{\varepsilon}_s^{\,(j,0)}(\vec{q})e^{\vec{q}\cdot\vec{R}^{(j,l)}}] = \frac{10}{\sqrt{16M_C}}\Re[\vec{\varepsilon}_s^{\,(j,0)}(\Gamma)] \tag{3.3.0.2}$$

being $N_{sc} = 16$ the number of atoms in the $2 \times 2 \times 2$ supercell.

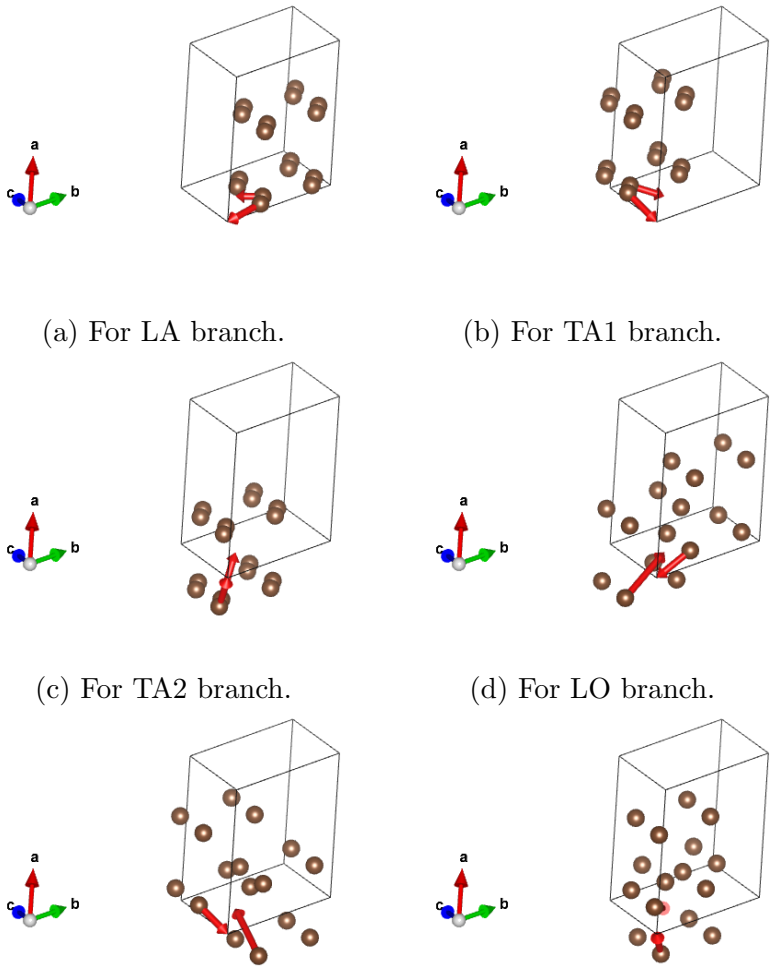

(a) For LA branch.

(b) For TA1 branch.

(c) For TA2 branch.

(d) For LO branch.

(e) For TO1 branch.

(f) For TO2 branch.

Figure 3.3: *3D visualization of the* $2 \times 2 \times 2$ *supercell structures undergoing modulated displacements along the six total normal modes in proximity of the k-point* Γ.

The first three 3.3a, 3.3b, 3.3c show in-phase oscillations within the unit cells and they are associated with the acoustic dispersion branches LA, TA1, TA2. While the other 3.3d, 3.3e, 3.3f involve counter-phase motions, that thus correspond to the optic dispersion branches LO, TO1, TO2.

3.4 Density of phonon states

The third step in the study of phononic properties of diamond Carbon consisted in calculating the total density of states $g(\omega)$ related to the previous *ab initio* dispersion branches in Figure 3.2 via the post-processing methods of Phonopy.
In particular, it requires the preparation of a configuration file named `pdos.conf`, which gets executed by the command

```
phonopy --cell=POSCAR-unitcell pdos.conf
```

and it is composed of the following basic statements

```
DIM = 2 2 2
ATOM_NAME = C

FULL_FORCE_CONSTANTS = .TRUE.
FORCE_CONSTANTS = READ

MP = 8 8 8
GAMMA_CENTER = .TRUE.
DOS = .TRUE.
```

The first four lines are equal to those in the configuration file `band.conf` shown in Section 3.3, while the others allow to count the number of phonon states with frequency $\omega_\lambda(\vec{q}^{\,(j)}) \simeq \omega$ where the symbol $\vec{q}^{\,(j)}$ indicates the j-th k-point of a Γ-centered mesh sampling of the first Brillouin zone, as explained in Section 3.2 and explicitly written in Equation (3.2.0.3).
The total density of phonon states function is thus calculated by Phonopy as

$$g(\omega) = \frac{1}{W} \sum_{\lambda,j} \delta(\omega - \omega_\lambda(\vec{q}^{\,(j)})) \tag{3.4.0.1}$$

such that satisfies the peculiar normalization condition

$$\int_0^\infty g(\omega) d\omega = 3N_{uc} \tag{3.4.0.2}$$

with W as the number of unit cells in the chosen supercell structure ($2\times2\times2$ or $3\times3\times3$) and $N_{uc} = 2$ as the number of atoms in the basis. The results of the execution of such a task are written in a DAT format file that can be easily read and plotted by a Python script, as illustrated in Figure 3.4 for both $2 \times 2 \times 2$ and $3 \times 3 \times 3$ supercell structures of diamond Carbon. These *ab initio* calculations are also compared to the experimental data in [12] through superposition.

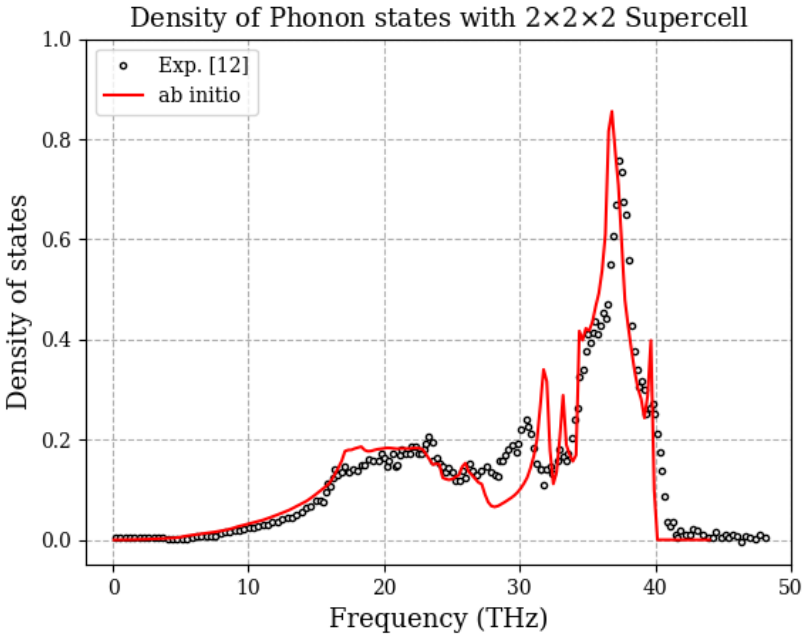
Density of Phonon states with 2×2×2 Supercell
Exp. [12]
ab initio
Density of states
Frequency (THz)
0.0
0.2
0.4
0.6
0.8
1.0
0
10
20
30
40
50

(a)

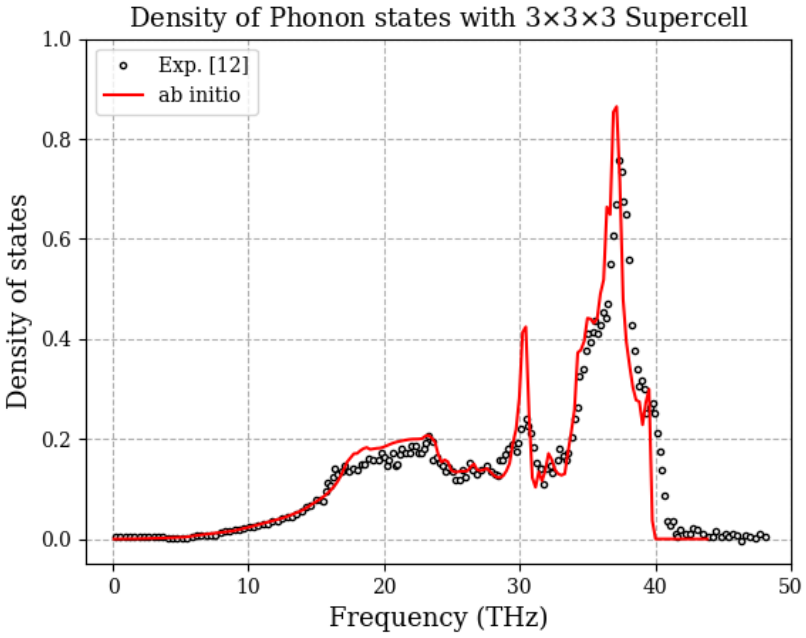
Density of Phonon states with 3×3×3 Supercell
Exp. [12]
ab initio
Density of states
Frequency (THz)
0.0
0.2
0.4
0.6
0.8
1.0
0
10
20
30
40
50

(b)

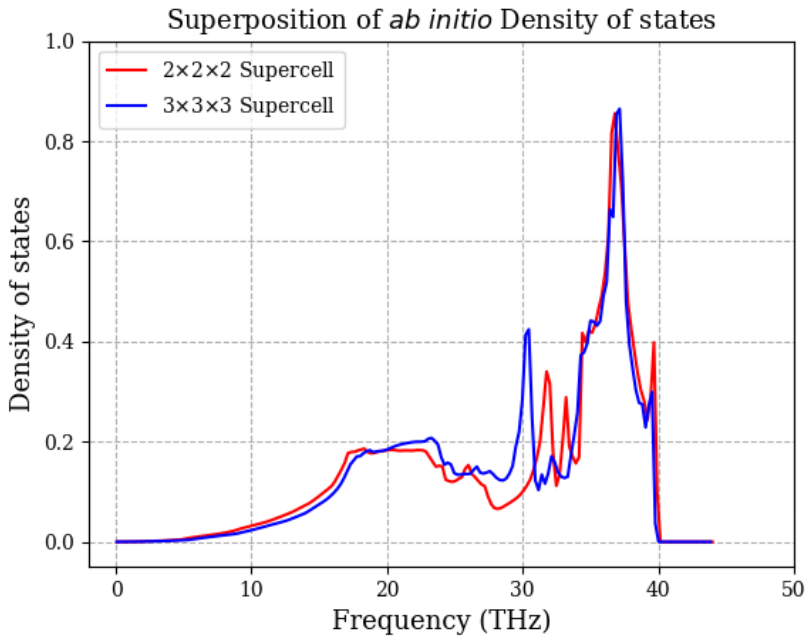

(c)

Figure 3.4: *Ab initio total density of phonon states for* $2\times2\times2$ (a) *and* $3\times3\times3$ *supercell structures* (b) *of fcc diamond Carbon overlapped with the experimental data in* [12]. *For better identifying the improvements between the two ab initio trends, their superposition graph is also reported* (c).

As in Section 3.3, the compatibility of the *ab initio* outcome to the experimental data increases remarkably with the size of the considered supercell during the procedure. In addition, they also exhibit very sharp van Hove singularities and a clear Debye trend ($\propto \omega^2$) in the low frequency limit due to the three acoustic dispersion branches.

3.5 Debye frequency evaluation

Due to the evident Debye trend ($\propto \omega^2$) in the low frequency limit for both experimental and *ab initio* data, two estimates of the Debye frequency ω_D of diamond Carbon have been calculated and then compared with each other in search of a possible accordance. The process aiming at obtaining them consists in fitting those two series of data to a curve of the form

$$g_{fit}(\omega) = B\omega^2 \tag{3.5.0.1}$$

in the frequency range $[0, \frac{1}{4}\omega_{max}]$, where ω_{max} is the maximum phonon frequency, which equals to 41.3 THz in the experimental case and to 40.3 THz in the other, and B is the fit parameter, whose final value at the same time ensures the normalization to $3N_{uc} = 6$ and allows to determine indirectly the Debye frequency via the relation

$$B = \frac{9N_{uc}}{\omega_D^3} \quad \rightarrow \quad \omega_D = \left(\frac{9N_{uc}}{B}\right)^{1/3}. \tag{3.5.0.2}$$

In particular, the fit parameter B has been measured to be

$$\begin{cases} B_{exp} = (1.38 \pm 0.22) \times 10^{-4} \text{ THz}^{-3} & \text{for experimental data} \\ B_{ai} = (1.68 \pm 0.26) \times 10^{-4} \text{ THz}^{-3} & \text{for } \textit{ab initio} \text{ data} \end{cases} \tag{3.5.0.3}$$

regarding the uncertainties ΔB_{exp}, ΔB_{ai} as the double value of the fit-estimated standard deviations $\sigma_{B,exp} = 0.11$ THz^{-3}, $\sigma_{B,ai} = 0.13$ THz^{-3}. Thus, the Debye frequency ω_D has been calculated as

$$\begin{cases} \omega_{D,exp} = (50.7 \pm 2.7) \text{ THz} & \text{for experimental data} \\ \omega_{D,ai} = (47.5 \pm 2.4) \text{ THz} & \text{for } \textit{ab initio} \text{ data} \end{cases} \tag{3.5.0.4}$$

where the uncertainties are obtained by a linear error propagation of ΔB_{exp}, ΔB_{ai} via the generic formula

$$\Delta\omega_D = \left|\frac{\partial\omega_D}{\partial B}\right| \Delta B = \frac{(9N_{uc})^{1/3}}{3B^{4/3}} \Delta B. \tag{3.5.0.5}$$

As a result, the definition of the derived quantity $\omega_{D,exp} - \omega_{D,ai}$ allowed to prove their reciprocal compatibility due to its indirect measurement

$$\omega_{D,exp} - \omega_{D,ai} = (3.2 \pm 5.1) \text{ THz} \tag{3.5.0.6}$$

that turns out to be consistent with its optimal value 0.
The plot of the final fitting curves is shown in Figure 3.5, where their domains are extended to the real interval $[0, \omega_D]$ in order to better visualize the global trend of the density of phonon states in the Debye approximation and its evident discrepancy in the high frequency limit with respect to both of the series of data.

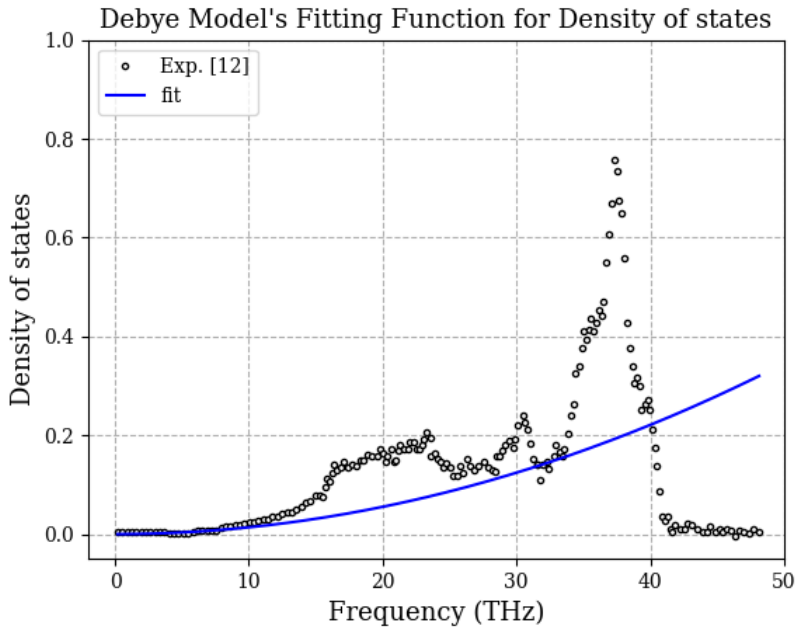

(a)

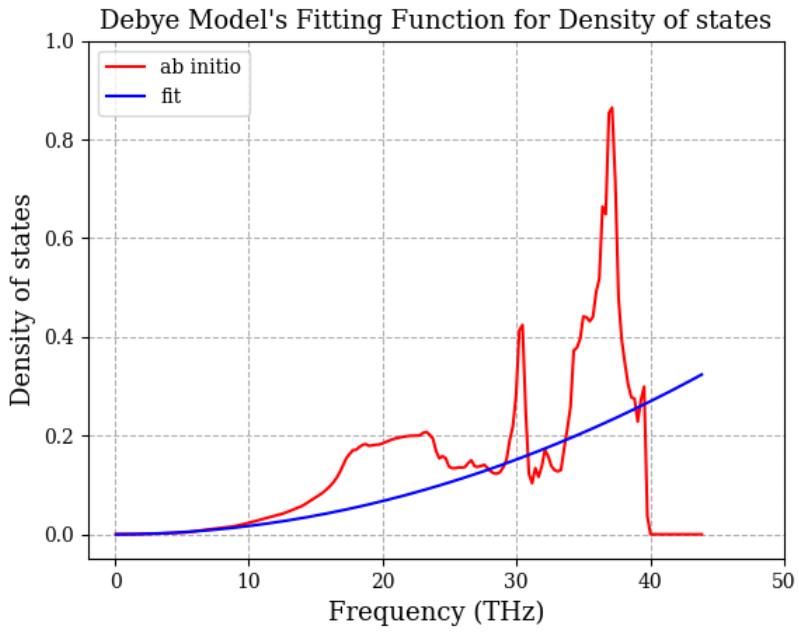

(b)

Figure 3.5: *Graphs of the best-fitting functions for the density of phonon states in the Debye approximation in relation to both experimental* (a) *and ab initio data* (b), *which are also overlapped to them.*

Chapter 4

Conclusion

The harmonic approximation of the vibrational modes of a solid crystal lattice is the foundation of the two most relevant theoretical models (Einstein and Debye ones), which provide an analytical solution for the temperature-dependent heat capacity function beginning with basic assumptions, as well as generically unrealistic, on the density of states function and the phononic dispersion relation.
Both their results agree with the classical Dulong-Petit law in the high temperature limit, but at the same time they also differ from that in the low one by showing a rapidly vanishing trend ($\propto \frac{1}{T^2}e^{-1/T}$ and $\propto T^3$ respectively for the Einstein and Debye models), which actually turns out to be more consistent with the related experimental data. This clearly demonstrates how necessary the quantum treatment of the 1D simple harmonic oscillator is with respect to the classical one.
However, their initial hypotheses are found to be valid only in limited conditions and frequency ranges. Indeed, the phononic dispersion relation for real solids cannot be considered to be linear generically because it actually presents acoustic and optic branches. The firsts set at 0 for $\vec{q} = \Gamma = (0, 0, 0)$ and in its vicinity they have a approximately linear trend, which makes them suitable for the Debye model in the low frequency, or high wavelength, limit. While the seconds exhibit a finite value even for $\vec{q} \to \Gamma$, and often show a nearly constant behaviour, which is instead a requirement of the Einstein model.
In addition, the number of branches in the phononic dispersion relation for real solids is proportional to the number of atoms in the unit cell N_{uc} of the 3D Bravais lattice under study with 3 as multiplier coefficient, but only three of them are acoustic, the others are all optic.
Furthermore, the density of phonon states function for 3D lattices presents sharp structures, called van Hove singularities, that violate the hypotheses of being Dirac delta shaped or quadratic, as respectively required by the Einstein and Debye models. In particular, these singularities arise from the cancellation condition of the denominator in the integral of Equation (2.6.0.2), which corresponds to the search for the critical points

$\vec{q}_{cp}$ of the phononic dispersion relation that thus satisfy $|\nabla_{\vec{q}}\, \omega_\lambda(\vec{q} = \vec{q}_{cp})| = 0$. On the basis of the characterization of such critical points, the van Hove singularities can be also classified into four types (M_0, M_1, M_2, M_3) and each of these involves a different behaviour of the associated part of the density of states, noting that because of the certain presence of acoustic dispersion branches a quadratic trend of the total function can be always observed in the low frequency limit.
Next, the VASP and Phonopy software allowed to compute from first principles some of the phononic properties of the fcc Bravais lattice of diamond Carbon starting from the ionic relaxation at an approximate minimum of the electronic energy to the evaluation of its specific Debye frequency. The main results concern though the *ab initio* calculation of the phononic dispersion curves and the total density of phonon states, both of which turned out to be consistent with the experimental data extracted from [11] and [12] respectively.
Moreover, the number and the quality of the so obtained dispersion branches is in accordance with the expectations for a 3D Bravais lattice with a diatomic basis, just like diamond Carbon.
At last, thanks to the quadratic trend of both experimental and *ab initio* data regarding the total density of phonon states in the low frequency limit, two compatible estimates of the Debye frequency for diamond Carbon (that are $\omega_{D,exp} = (50.7 \pm 2.7)$ THz and $\omega_{D,ai} = (47.5 \pm 2.4)$ THz) have been calculated by executing curve fitting operations limited to the two intervals $[0, \frac{1}{4}(41.3 \text{ THz})]$ and $[0, \frac{1}{4}(40.3 \text{ THz})]$ respectively.

Bibliography

[1] M. Maldovan. "Sound and heat revolutions in phononics". In: *Nature* 503 (2013). DOI: https://doi.org/10.1038/nature12608.

[2] Neil W. Ashcroft and N. David Mermin. *Solid State Physics*. Harcourt Inc., 1976. ISBN: 0030839939.

[3] Malcolm P. Kennett. *Essential Statistical Physics*. Cambridge University Press, 2020. ISBN: 9781108480789.

[4] Stephen J. Blundell and Katherine M. Blundell. *Concepts in Thermal Physics*. Oxford University Press Inc., 2010. ISBN: 9780199562091.

[5] Marvin L. Cohen and Steven G. Louie. *Fundamentals of Condensed Matter Physics*. Cambridge University Press, 2016. ISBN: 9780521513319.

[6] G. Kresse and J. Hafner. "Ab initio molecular-dynamics simulation of the liquid-metal-amorphous-semiconductor transition in germanium". In: *Physical Review B* 49 (1994). DOI: https://doi.org/10.1103/PhysRevB.49.14251.

[7] G. Kresse and J. Furthmümuller. "Efficiency of ab-initio total energy calculations for metals and semiconductors using a plane-wave basis set". In: *Computational Materials Science* 6 (1996), pp. 15–50. DOI: https://doi.org/10.1016/0927-0256(96)00008-0.

[8] G. Kresse and J. Furthmümuller. "Efficient iterative schemes for ab initio total-energy calculations using a plane-wave basis set". In: *Physical Review B* 54 (1996). DOI: https://doi.org/10.1103/PhysRevB.54.11169.

[9] A Togo and I Tanaka. "First principles phonon calculations in materials science". In: *Scr. Mater.* 108 (2015), pp. 1–5. DOI: http://dx.doi.org/10.1016/j.scriptamat.2015.07.021.

[10] Feliciano Giustino. *Materials modelling using Density Functional Theory*. Oxford University Press Inc, 2014. ISBN: 9780199662449.

[11] Gian-Marco Rignanese Xavier Gonze and Razvan Caracas. "First-principle studies of the lattice dynamics of crystals, and related properties". In: *Zeitschrift für Kristallographie* (2005). DOI: https://doi.org/10.1524/zkri.220.5.458.65077.

[12] Alexey Bosak and Michael Krisch. "Phonon density of states probed by inelastic x-ray scattering". In: *Physical Review B* (2005). DOI: https://doi.org/10.1103/PhysRevB.72.224305.

[13] G. Nilsson and S. Rolandson. "Lattice Dynamics of Copper at 80 K". In: *Physical Review B* 7 (2014). DOI: https://doi.org/10.1103/PhysRevB.7.2393.

[14] D. Broido L. Lindsay and T. L. Reinecke. "Ab initio thermal transport in compound semiconductors". In: *Physical Review B* 87 (2013). DOI: https://doi.org/10.1103/PhysRevB.87.165201.

[15] K. Momma and F. Izumi. "An integrated three-dimensional visualization system VESTA using wxWidgets". In: *Commission on Crystallographic Computing, IUCr Newsletter* 7 (2006).

[16] K. Momma and F. Izumi. "Three-Dimensional Visualization in Powder Diffraction". In: *Solid State Phenomena* 130 (2007). DOI: https://doi.org/10.4028/www.scientific.net/SSP.130.

[17] K. Momma and F. Izumi. "VESTA: a three-dimensional visualization system for electronic and structural analysis". In: *Journal of Applied Crystallography* 41 (2008). DOI: https://doi.org/10.1107/S0021889808012016.

[18] K. Momma and F. Izumi. "VESTA 3 for three-dimensional visualization of crystal, volumetric and morphology data". In: *Journal of Applied Crystallography* 44 (2011). DOI: https://doi.org/10.1107/S0021889811038970.

[19] J. D. Hunter. "Matplotlib: A 2D graphics environment". In: *Computing in Science & Engineering* 9.3 (2007), pp. 90–95. DOI: 10.1109/MCSE.2007.55.

[20] Charles R. Harris et al. "Array programming with NumPy". In: *Nature* 585 (2020), 357–362. DOI: 10.1038/s41586-020-2649-2.

[21] Pauli Virtanen et al. "SciPy 1.0: Fundamental Algorithms for Scientific Computing in Python". In: *Nature Methods* 17 (2020), pp. 261–272. DOI: 10.1038/s41592-019-0686-2.